



Numerical modelling of tsunami propagation in idealised converging water body geometries

Zhiwen Chen^{*}, Valentin Heller, Riccardo Briganti

Environmental Fluid Mechanics and Geoprocesses Research Group, Faculty of Engineering, Nottingham, NG7 2RD, UK

ARTICLE INFO

Keywords:

Converging water body
Non-linear wave interaction
Stem wave
SWASH
Tsunamis

ABSTRACT

Tsunamis have caused many severe natural disasters in human history, such as in 2018 at Palu City located in a narrow bay resulting in over 4340 fatalities. The tsunami propagation characteristics are greatly affected by the water body geometry. For converging geometries such as fjords, bays and estuaries, the interaction between incident tsunamis and lateral boundaries has not been extensively studied. Therefore, the propagation of approximately linear, Stokes, cnoidal and solitary waves are studied numerically in converging, uniform depth water bodies with side angles of 7.5°, 15°, 30° and 45°. Both curved (without sidewall reflection) and straight wave sources (involving sidewall reflection) are used. SWASH, an open-source numerical wave propagation model based on the non-hydrostatic non-linear shallow water equations, is used. For a curved wave source, the wave heights H closely follow Green's law and doubled as the water body width converged to 25% of the original width. However, for wide geometries with a straight wave source, due to reflections from the converging walls, Greens law is inappropriate to predict H . Wave energy can be concentrated on the sides or laterally transferred from stem wave growth and interaction, producing much larger H than predicted by Greens law. The water body width relative to the water depth h is found to have a significant effect on this transformation. Solitary wave amplitudes from 0.100 to 0.623 times h are simulated. An equation is derived for the solitary wave amplitude in a converging water body and an empirical equation is proposed for the prediction of the stem angle. A method for evaluating wave amplification at sidewalls is further presented and compared with the simulation results of this study. Finally, the application of this method is illustrated with an example inspired by the 2018 Palu Bay event. These findings enhance the physical understanding of the effect of the converging water body geometry on tsunami propagation and improve tsunami prediction and hazard assessment.

1. Introduction

Tsunamis are long gravity waves caused by the displacement of a large volume of water, e.g. by tectonic movements or landslides. Tsunamis with large energy are serious threats to passing ships, dams and buildings, and are sometimes the source of devastating disasters (Mori et al., 2011; Goda et al., 2019; Heller and Ruffini, 2023; Romano et al., 2023). During wave propagation, a series of transformations occur: wave shoaling, refraction, diffraction, reflection and wave breaking. The bathymetry and water body geometry affect the wave height, wavelength and wave direction, amongst other wave characteristics (Knowles and Yeh, 2018; Ruffini et al., 2019, 2021; Zhang et al., 2020). The conventional practice for generic studies is to use idealised geometries (Heller and Ruffini, 2023). Several previous studies showed that the effects of the bathymetry and water body geometry on tsunamis are significant (Heller et al., 2012; Romano et al.,

2013; Evers et al., 2019; Franco et al., 2021; Wuppukondur and Bal-dock, 2022; Chen et al., 2023). However, compared to other scenarios, tsunami hazard prediction tools for propagation in converging water bodies are still underdeveloped.

As an example of a converging water body geometry, Fig. 1 shows Palu Bay, affected by the 2018 Sulawesi earthquake and tsunami. The Pantoloan tidal gauge recorded a wave height of up to 3.81 m (Pakok-sung et al., 2019; Pudjaprasetya et al., 2021; Cecioni et al., 2023). Heidarzadeh et al. (2019) estimated the wavelength to be between 3.4 and 4.1 km, whereas the Palu Bay is 9.4 km wide and over 30 km long. This event caused severe damage to Palu City located at the end of this narrow bay, with over 4340 fatalities, 4438 injuries and widespread destruction of infrastructure and buildings (Goda et al., 2019; Kraut-wald et al., 2021). The geometry of Palu Bay can be simplified as a symmetric water body with the side angle $\theta = 7.5^\circ$ (Fig. 1). Note that

^{*} Corresponding author.

E-mail address: Zhiwen.Chen@nottingham.ac.uk (Z. Chen).

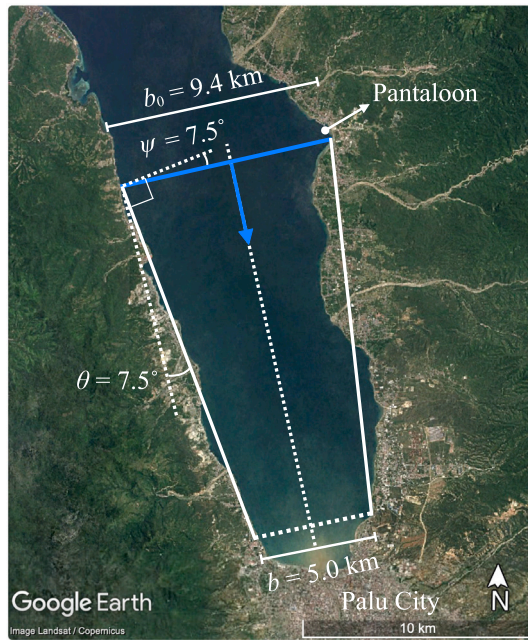


Fig. 1. Satellite picture of Palu Bay and Palu City affected by the 2018 tsunami as an example of a converging water body.
Source: Adapted from Google Earth.

when the tsunami propagates along the axis of symmetry towards the converging direction of the water body, it will impact the sidewalls at an oblique angle ψ of the same value as θ . Further severe tsunamis in various water bodies include the 2014 Lake Askja tsunami, triggered by a rockslide, which reached a run-up of 71 m with a wavelength of approximately 1 km within a basin that is around 3.8 km in width and 5.0 km in length (Gylfadóttir et al., 2017). Additionally, in 1958, an 8.3 magnitude earthquake triggered a rockslide in Lituya Bay, generating a soliton-like wave that ran up to a height of 524 m with a wavelength of approximately 3 km (Fritz et al., 2001). Lituya Bay itself is about 3.3 km wide and 12.0 km long in the direction of the slide. To cover a wide range of scenarios, water body geometries with different θ and sizes should be considered systematically. The effect of a converging water body geometry on tsunamis and the resulting wave field remains inadequately understood due to limited systematic studies. Therefore, this paper aims to elucidate this impact by exploring the associated underlying physical phenomena for idealised converging geometries.

Theoretically, the change in wave height H of non-breaking shallow water waves propagating in water body geometries with decreasing water depth h and varying width b can be described by Greens law (Green, 1838), which is based on the conservation of the wave energy flux between two cross-sections, given by

$$\frac{H}{H_0} = \left(\frac{h_0}{h}\right)^{1/4} \left(\frac{b_0}{b}\right)^{1/2}, \quad (1)$$

where the subscript 0 refers to the initial or reference state. Chang et al. (1979) investigated the propagation of solitary waves in a converging and a diverging flume, with one of the lateral walls at a side angle of $\theta = 1.1^\circ$ and a constant h . They found that for a relative distance $x/h < 40$, the wave height H can be approximated using Greens law. Furthermore, Xian-chu (1981) derived a relation between H of solitary waves and the size of the water body using Korteweg-de Vries (KdV) solutions, which was found to perform more accurately than Greens law as it considers non-linear effects. For water bodies with rectangular cross-sections, this equation is given as

$$\frac{H}{H_0} = \frac{h_0}{h} \left(\frac{b_0}{b}\right)^{2/3}. \quad (2)$$

Landslide-tsunami generation and propagation in a range of idealised diverging geometries were investigated for the first time in the small-scale laboratory study of Heller et al. (2012). Diverging idealised geometries with water body side angles $\theta = 7.5^\circ, 15^\circ, 30^\circ$ and 45° were later also investigated numerically by Heller et al. (2016) for subaerial landslide-tsunamis using Smoothed Particle Hydrodynamics (SPH). A more systematic numerical investigation with different wave types, including linear, Stokes, cnoidal and solitary waves, was reported by Ruffini et al. (2019) with similar θ as in Heller et al. (2016). They quantified the effect of the water body geometry and presented a method to predict H based on wave parameters in Two-Dimensional (2D) flume geometries, where the 2D parameters are available from studies such as Heller and Hager (2010), Zitti et al. (2016) or Xue et al. (2019).

In contrast to diverging water body geometries, waves propagation in converging geometries involves reflection from the sidewalls. Perroud (1957) conducted experiments and observed that when $45^\circ < \psi < 90^\circ$, a wave pattern similar to regular reflection emerged, as shown in Fig. 2a. The reflected wave maintains the characteristics of the incident one, such as a reflected amplitude a_r and angle ψ_r . In this case, a stem or hump forms after the wave impingement and remains stable thereafter. However, for smaller angles (e.g. $20^\circ \leq \psi \leq 40^\circ$ in Li et al., 2011), a continuously growing stem forms perpendicularly to the wall for non-linear waves (Fig. 2b). A specific physical phenomenon is called Mach reflection in which a solitary wave interacts with a vertical wall at a sufficiently small angle. This interaction creates a reflected wave that intersects with the incident wave and results in the formation of a high-amplitude Mach stem wave (Perroud, 1957; Miles, 1977a,b; Li et al., 2011). As shown in Fig. 2b, the so-called stem length l_s increases with a gradient determined by the stem angle ψ_w as the wave propagates. Note that l_s increases linearly, while the stem wave amplitude a_w does not. The rate at which a_w is amplified decreases, approaching a theoretical asymptotic value as the process continues. For example in the numerical study of Li et al. (2011), the distance required to reach 95% of the asymptotic amplification is $103.8h$ for an incident solitary wave with a relative amplitude $a/h = 0.277$ and $\psi = 30^\circ$.

The prediction equations for Mach reflection a_w and ψ_w in the asymptotic state were first derived for KdV solitons by Miles (1977a) with the assumption of shallow water conditions, small wave amplitude and a small oblique angle. The stem wave amplification $\alpha_w = a_w/a$ and ψ_w (in radians) are given by

$$\alpha_w = \begin{cases} \frac{4}{1 + \sqrt{1 - K^{-2}}}, & \text{for } K \geq 1, \\ (1 + K)^2, & \text{for } K < 1, \end{cases} \quad (3)$$

$$\psi_w = \begin{cases} 0, & \text{for } K \geq 1, \\ \sqrt{\frac{a}{3h}}(1 - K), & \text{for } K < 1, \end{cases} \quad (4)$$

where K is the interaction parameter, defined as $K = \psi/\sqrt{3a/h}$. At $K = 1$, the maximum value of α_w is 4, with a regular reflection pattern observed when $K > 1$ (Fig. 2a) and a Mach reflection when $K < 1$ (Fig. 2b). Based on the Kadomtsev-Petviashvili (KP) theory, Kodama et al. (2009) modified this critical condition to $K_K = \tan \psi / (\cos \psi \sqrt{3a/h})$, which was experimentally verified by Li et al. (2011). More recently, Kodama and Yeh (2016) derived $K_{KY} = \tan \psi \sqrt{1 + \sqrt{1 + 5a/h}} / (\cos \psi \sqrt{6a/h})$ of the KP equation with higher-order corrections. In a numerical simulation, Knowles and Yeh (2019) achieved $\alpha_w = 3.91$ for $\psi_w = 10^\circ$ and $a/h = 0.01$ ($K_{KY} = 1.0$). However, approaching this asymptotic state requires a considerable amount of time (e.g. approximately 14 h of real time for the $h_0 = 1$ m case). In practice, there is a lack of analytical solutions addressing the stage of stem wave growth. In general, Mach reflection has important implications for coastal engineering and tsunami hazard assessment, as

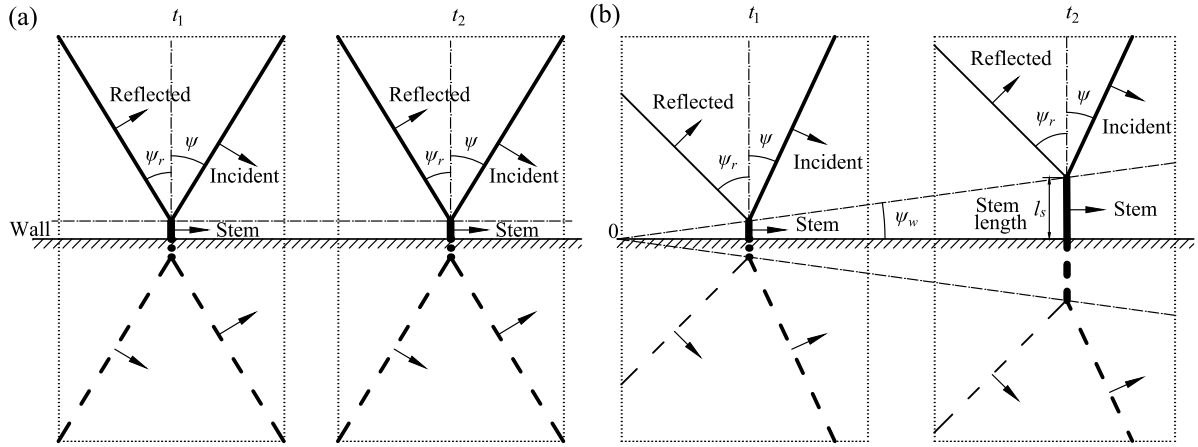


Fig. 2. Schematic plan views of the evolution of an incident solitary wave interacting with the wall obliquely at two different times t_1 and t_2 ($t_1 < t_2$): (a) regular reflection and (b) Mach reflection. The widths of the lines representing the wave crests are indicative of the size of the wave amplitudes. When an incoming wave impinges onto a reflective wall, the interaction can be considered as the interaction between the wave itself (solid lines) and its image (dashed lines) reflected about the axis of the wall as the frictionless boundary conditions of the wall align with the conditions on the symmetric plane.

it can amplify wave heights with potential significant damage inland, particularly in converging water body geometries (Gidel et al., 2017).

To better understand tsunami propagation in converging geometries, Wuppukondur and Baldock (2022) studied solitary and bore wave propagation and overtopping in a converging channel with $\theta = 5^\circ$, both experimentally and numerically. They found that, in the absence of overtopping, the solitary wave height variation is consistent with Greens law. However, they investigated a converging channel with a single-side oblique wall and did not vary θ . Therefore, further work is needed to study more general cases with both sidewalls oblique and a wide range of geometries with different θ .

To this end, the present study numerically addresses tsunami-like waves propagation in converging water body geometries using SWASH (Zijlema et al., 2011; Ruffini et al., 2019), based on the non-hydrostatic Non-Linear Shallow Water Equations (NLSWEs). The objectives of this study are to

- Investigate the effect of converging water body geometries with curved and straight wave sources on tsunami-like waves propagation,
- Improve the physical understanding of solitary wave propagation in converging geometries with straight wave sources and straight side walls,
- Provide a new efficient prediction method accounting for the effect of a wide range of water body side angles to improve tsunami prediction and hazard assessment.

The remainder of this article is organised as follows. Section 2 provides information about the numerical setup, including the calibration and validation of the SWASH model. The results of the simulations for both curved and straight wave sources are presented in Section 3 along with new equations for the prediction of ψ_w and wave amplification. In Section 4 the results are analysed and a prediction method for evaluating wave amplification at the sidewalls is presented and illustrated with an example. Finally, Section 5 highlights the conclusions and potential future work.

2. Methodology

2.1. Wave propagation model

SWASH v7.01, solving the non-hydrostatic NLSWEs (Stelling and Duijnmeijer, 2003; Stelling and Zijlema, 2003; Zijlema and Stelling, 2005; Zijlema et al., 2011), is used to simulate the propagation of

tsunamis in converging water body geometries. The mass and momentum conservation equations are:

$$\frac{\partial \eta}{\partial t} + \bar{u} \frac{\partial d \bar{u}}{\partial x} + \bar{v} \frac{\partial d \bar{v}}{\partial y} = 0, \quad (5)$$

$$\frac{\partial \bar{u}}{\partial t} + \bar{u} \frac{\partial \bar{u}}{\partial x} + \bar{v} \frac{\partial \bar{u}}{\partial y} + g \frac{\partial \eta}{\partial x} + \frac{1}{d} \int_{-h}^{\eta} \frac{\partial q}{\partial x} dz + c_f \frac{\bar{u} \sqrt{\bar{u}^2 + \bar{v}^2}}{d} = \frac{1}{d} \left(\frac{\partial d \tau_{xx}}{\partial x} + \frac{\partial d \tau_{xy}}{\partial y} \right), \quad (6)$$

$$\frac{\partial \bar{v}}{\partial t} + \bar{u} \frac{\partial \bar{v}}{\partial x} + \bar{v} \frac{\partial \bar{v}}{\partial y} + g \frac{\partial \eta}{\partial y} + \frac{1}{d} \int_{-h}^{\eta} \frac{\partial q}{\partial y} dz + c_f \frac{\bar{v} \sqrt{\bar{u}^2 + \bar{v}^2}}{d} = \frac{1}{d} \left(\frac{\partial d \tau_{yx}}{\partial x} + \frac{\partial d \tau_{yy}}{\partial y} \right), \quad (7)$$

where t is the time and x , y and z are the coordinates with the origin located at the still water surface. η is the free surface elevation measured from the still water level and $d = h + \eta$ is the total water depth. \bar{u} and \bar{v} are the depth-averaged flow velocity components in the x and y direction, respectively. The non-hydrostatic pressure term q is a component of the total pressure p_t (Zijlema and Stelling, 2005), defined as

$$p_t = g(\eta - z) + q. \quad (8)$$

τ_{xx} , τ_{xy} , τ_{yx} and τ_{yy} are the horizontal turbulent stresses, $g = 9.81 \text{ m/s}^2$ is the gravitational acceleration and c_f is the dimensionless bottom friction coefficient based on Manning's roughness coefficient n , defined as

$$c_f = \frac{n^2 g}{d^{1/3}}, \quad (9)$$

where $n = 0.009 \text{ s/m}^{1/3}$ was selected in all geometries in this study to simulate a typical flume made of glass. The time integration with the explicit method in SWASH is regulated by the Courant–Friedrichs–Lewy (CFL) condition to obtain a stable solution (SWASH, 2020). The CFL condition, in terms of Courant number C_r , is

$$C_r = \Delta t (\sqrt{gd} + \sqrt{u^2 + v^2}) \sqrt{\frac{1}{\Delta x^2} + \frac{1}{\Delta y^2}} \leq 1, \quad (10)$$

where u and v are the flow velocity components in the x and y direction. Δx and Δy are the distances between two points of adjacent cells in the x and y directions, respectively. The time step Δt is dynamically adjusted to satisfy Eq. (10), with a minimum (subscript *min*) value of $C_{r,min} \leq 0.1$ and a maximum (subscript *max*) value of $C_{r,max} = 0.5$ in this study.

A major advantage of the SWASH model is that a low vertical resolution (e.g. 2 layers) is sufficient to accurately describe refraction, shoaling, diffraction and non-linear wave–wave interaction (SWASH, 2020).

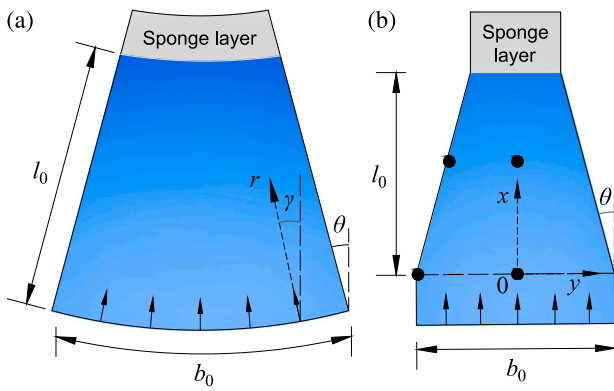


Fig. 3. Profiles of investigated convergent water body geometries with $\theta = 15^\circ$: (a) curved and (b) straight wave sources with four gauges (black points) for the convergence tests.

To account for wave breaking in converging water bodies with flat bottoms, a hydrostatic computation approach was adopted in SWASH, which divides the computational domain into two layers and enables wave breaking with conservation of mass and momentum, providing a similar effect to a higher vertical resolution typically required for wave breaking (10 ~ 20 layers). The Keller-box scheme (Lam and Simpson, 1976) is used as it gives good dispersive properties for two equidistant layers (maximum error 1% with $kh \leq 7.7$, where k is the wave number).

Parallel computing using the Message Passing Interface (MPI) standard is used by SWASH, reducing the simulation time of the Central Processing Unit (CPU) calculations in this study. The High Performance Computing (HPC) Augusta of the University of Nottingham is used in this study, featuring 2×20 core processors (Intel Skylake 6138 2.0 GHz) per node. Most simulations are conducted using a single node.

2.2. Numerical domain and boundary conditions

This study simplifies the modelling by considering symmetric tsunami propagation in a converging water body to preliminarily investigate the underlying physical phenomena associated with far-field tsunami generation or for tsunamis generated by a landslide with a width that exceeds the width of the converging water body entering e.g. narrow fjords or lakes sections (Løvholm et al., 2015; Hilbe and Anselmetti, 2015). Two wave source shapes are used in the investigated symmetric water bodies (Fig. 3), namely curved (without sidewall reflection) and straight (involving sidewall reflection). The waves generated by both wave sources propagated in converging water bodies with side angles $\theta = 7.5^\circ, 15^\circ, 30^\circ$ and 45° . The default unit for angles herein is radians, including trigonometric functions, unless it is explicitly stated as degrees ($^\circ$). Although the governing equations are formulated in Cartesian coordinates, for the purpose of representation, polar coordinates are introduced to depict the radial propagation of incident waves in geometries with a curved wave source (Fig. 3a). This allows for a more intuitive visualisation of the wave behaviour in a converging water body geometry with a length of l_0 , using the coordinate system (r, γ) . The parallel incident wave generated by a straight wave source propagates through a uniform width portion of the domain, with a length of 6 m, and reaches the origin of the Cartesian coordinate system (x, y) . This is followed by a converging water body with local width $b = b_0 - 2x \tan \theta$, where b_0 is the initial width and also the length of the wave source. The corresponding width for the radial incident waves is $b = b_0 - 2r\theta$. The curvature of the wave source is $\lambda = 2\theta/b_0$.

Structured grids, similar as in Ruffini et al. (2019), were generated in Delft3D and used in this study. The number of grid cells in the x and y directions was 1152×768 ($x \times y$) for all geometries.

Convergence tests for other resolutions are addressed in Section 2.3.1. The quality of the curvilinear grids is determined by the degree of orthogonality, which is defined as the difference between the angle of intersecting grid lines and 90° (SWASH, 2020), where zero indicates perfectly orthogonal grid lines. The reason for extending the numerical domain for geometries with straight wave sources is to improve the orthogonality of the grids at the intersection of the rectangular and converging part of the domain. In all computational domains of this study, the value of orthogonality is less than 0.04 with smooth corners if needed. Furthermore, the variation in the size of two adjacent cells is ≤ 1.1 based on the smoothness parameter.

The wave parameters and water depth h for all considered wave types are summarised in Table 1. An approximated linear wave with a height $H = 0.040$ m, period $T = 0.876$ s and wavelength $L = 1.19$ m, in a water depth of $h = 0.60$ m, was considered (Ruffini et al., 2019). The present study also involved non-linear Stokes (Fenton, 1985), cnoidal (Fenton, 1999) and solitary waves (Boussinesq, 1872), based on wave parameters measured in the subaerial landslide-tsunamis study of Heller and Hager (2011). To validate the capability of modelling Mach reflection, the solitary wave with $a/h = 0.277$ used in Li et al. (2011) was also generated by a straight wave source. Solitary waves with different a were considered to examine the variation of the stem-wave angle ψ_w . However, when a/h was large (e.g. $a/h = 0.75$), the wave speed c of the 1st order Boussinesq solution showed a non-negligible error due to the unstable solitary wave generation in SWASH. Thus, the algorithm developed by Teng (1997) for the exact Boussinesq solution (Teng and Wu, 1992) was used to generate solitary waves with $a/h = 0.75$. Apart from the wavelength from Heller and Hager (2011), an effective wavelength of $4.24a^{-1/2}h^{3/2}$, including 95% of the wave volume (Dean and Dalrymple, 1991), was computed for the remaining theoretical solitary waves.

The water surface time series of each wave type were used as the input for SWASH on the finite wave generation boundary. To simulate incident waves without reflections at the offshore boundary, a weakly reflective condition, allowing outgoing waves, was adopted. In addition, a ramping-up function was used to simulate a smooth initial stage of the wave train to avoid numerical instabilities. The analysis only started once a stable wave height was reached. The wave height decay due to bottom friction is negligible (e.g. 0.13% over 6 m for solitary waves). A sponge layer with a length of at least $2L$ was added at the end of the converging water bodies to absorb the waves.

2.3. Calibration and validation

A case based on the 1st order solitary wave theory and wave parameters measured in Heller and Hager (2011) was replicated in a uniform flume to validate the results of SWASH v4.01 in Ruffini et al. (2019). Enabling the momentum conservation command in SWASH v7.01 (which is applied by default in v4.01) resulted in identical results between the two versions. In the present study, wave breaking was enabled, which is a key difference from Ruffini et al. (2019). Once wave breaking with 2 vertical layers is enabled in SWASH, certain approximations on non-hydrostatic pressure (vertical accelerations are not resolved) are made for the grid point located in front of a breaking wave (SWASH, 2020). Herein, wave breaking is initiated when the local surface steepness $\partial\eta/\partial t > 0.6\sqrt{gh}$. Additionally, both the second-order Backward Differentiation Formula (BDF) scheme (calibrated in Ruffini et al., 2019) and the Central Differentiation Formula (CDF) scheme (recommended option for enabling breaking in SWASH, 2020) were tested. Using the BDF for the non-breaking solitary wave made essentially no difference compared to the CDF scheme. However, for the BDF scheme, when Mach reflection occurs in a geometry with straight wave sources, the incident wave broke without steepening once the amplified stem wave started breaking. Wave breaking and the CDF scheme were therefore applied for simulations of straight wave sources, while simulations with curved wave sources relied on the BDF scheme.

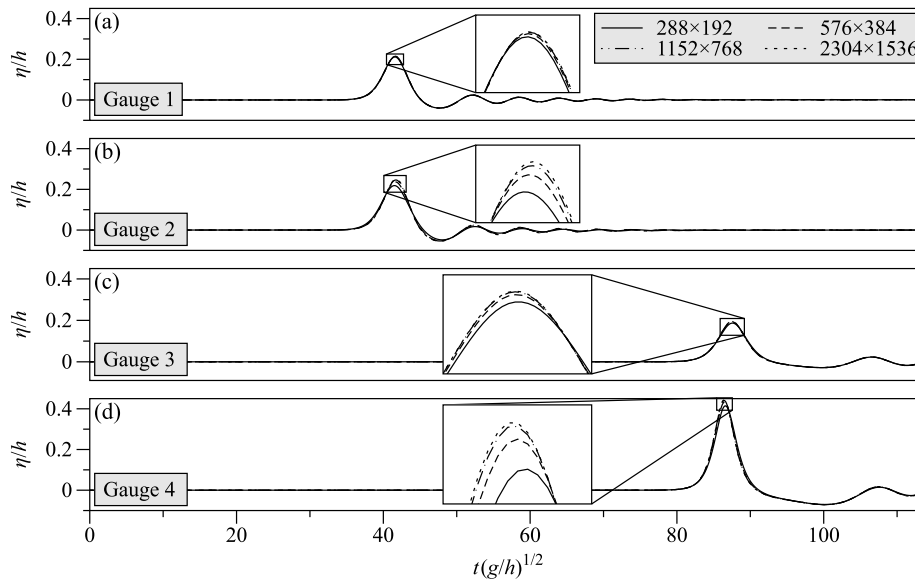


Fig. 4. Convergence tests for the solitary wave profile with $a/h = 0.277$ in the geometry with $\theta = 30^\circ$.

Table 1
Wave parameters of all simulations.

Wave type	h (m)	H (m)	T (s)	L (m)	a (m)	c (m/s)	Wave source
Approximate linear (Ruffini et al., 2019)	0.600	0.040	0.876	1.190	–	–	Curved
5th order Stokes (Fenton, 1985; Heller and Hager, 2011)	0.600	0.100	1.000	1.530	–	–	Curved
5th order cnoidal (Fenton, 1999; Heller and Hager, 2011)	0.300	0.155	1.740	2.830	0.110	1.630	Curved
1st order solitary (Boussinesq, 1872; Heller and Hager, 2011)	0.300	0.159	–	2.823	0.159	1.969	Curved and straight
1st order solitary (Goring, 1979; Li et al., 2011)	0.300	0.083	–	2.322	0.083	1.939	Straight
1st order solitary (Boussinesq, 1872)	0.300	0.030	–	4.022	0.030	1.799	Straight
		0.060	–	2.844	0.060	1.879	
		0.090	–	2.322	0.090	1.956	
Solitary (Teng, 1997)	0.300	0.120	–	2.011	0.120	2.030	Straight
		0.225	–	1.469	0.225	2.213	

2.3.1. Convergence tests

To assess grid convergence, multiple resolutions were examined for a geometry with a straight wave source and $\theta = 30^\circ$ and $b_0 = 60$ m. Four wave gauges were used to compare the solitary wave with $a/h = 0.277$: gauge 1 ($x = 0$ m, $y = 0$ m), 2 (0 m, 29.97 m), 3 (15 m, 0 m) and 4 (15 m, 21.35 m), indicated by black circles in Fig. 3. Gauges 2 and 4 were placed at the sidewall to measure stem wave convergence. Various resolutions were tested, namely 288×192 , 576×384 , 1152×768 and 2304×1536 meshes. Fig. 4 shows the relative water surface elevation η/h versus the normalised time $t(g/h)^{1/2}$ at gauges 1 to 4. From the zoomed wave profiles, the free surface at gauges 2 and 4, where amplified stem waves are observed, are more sensitive to the resolution in the tested range than incident waves at gauges 1 and 3.

Table 2 quantifies a for a solitary wave at the four resolutions, and their relative error ϵ in percentage, defined as the difference between 1 and the ratio of a of the lower to the nearest higher resolution case. To achieve the same degree of convergence, stem waves (Fig. 4b and d) require a higher resolution than incident waves in the centre (Fig. 4a

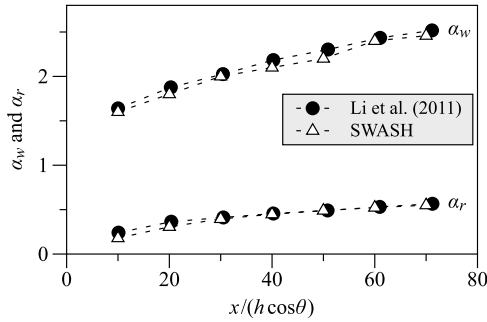
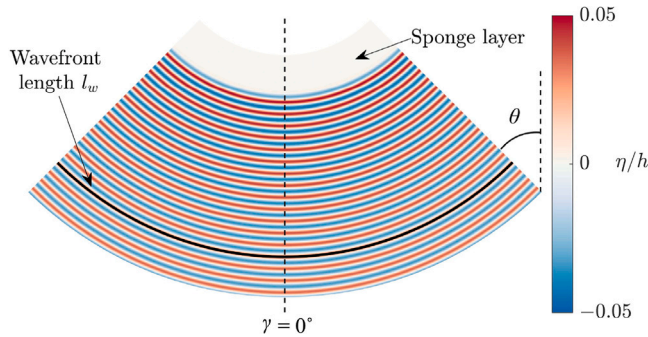
and c). For the resolution 2304×1536 , the model took approximately 33 h of real time to simulate 60 s using 40 CPU cores (Table 2). Between 1152×768 and 2304×1536 , even the largest $\epsilon = 1.68\%$ is small, and considering the computational cost and unstable excessive grid refinement (Zijlema, 2020), the use of 1152×768 is considered appropriate for the main tests of the current study.

2.3.2. Validation for mach reflection

A laboratory experiment from Li et al. (2011) was used to validate the simulation of Mach reflection of a solitary wave $a/h = 0.277$ obliquely interacting with a vertical wall with $\theta = 30^\circ$. The meniscus effect is limited to a distance smaller than $0.167h$ from the wall and does not affect the rest of the profiles (Li et al., 2011). Therefore, on a macroscopic level, it can be neglected, such that the sidewall is modelled as frictionless in the SWASH model. The reflected wave amplification is $\alpha_r = a_r/a$ with a_r as the reflected wave amplitude. Fig. 5 shows the development of α_w and α_r with relative stem wave propagation distance $x/(h \cos \theta)$ along the sidewall. The results of α_w and α_r are both consistent with the experiments but slightly smaller.

Table 2Comparison of results for different grid resolutions for the solitary wave with $a/h = 0.277$ in the geometry with $\theta = 30^\circ$.

Resolution	Gauge 1		Gauge 2		Gauge 3		Gauge 4		Time (min)
	a/h	ϵ (%)							
288×192	0.2114	0.98	0.2185	7.61	0.1868	3.06	0.4144	4.27	21
576×384	0.2135	0.47	0.2365	3.94	0.1927	1.23	0.4329	1.79	84
1152×768	0.2145	0.09	0.2462	1.68	0.1951	0.26	0.4408	0.47	336
2304×1536	0.2147	–	0.2504	–	0.1956	–	0.4429	–	1977

**Fig. 5.** Amplification growth of the stem wave α_w and the reflected wave α_r from a solitary wave $a/h = 0.277$ in a geometry with $\theta = 30^\circ$.**Fig. 6.** Plan view of relative water surface elevation η/h for approximate linear waves in a geometry with the curved wave source and $\theta = 45^\circ$ at $t = 50$ s.

3. Results

3.1. Curved wave source

An idealised curved wavefront is first investigated as a relatively simple case. This may occur in nature when a straight wavefront interacts with a shoal. The curved wave source ensured the propagation of radial incident waves without reflection from the converging sidewalls, resulting in a uniform wave height distribution across the wavefront (Fig. 6). Therefore, unless specified, the analysed parameters of waves along the symmetry line ($\gamma = 0^\circ$) are presented in Section 3.1. Specifically, the time series of η and H are investigated for the linear, Stokes, cnoidal and solitary waves in geometries with $b_0 = 60$ m and $\theta = 7.5^\circ, 15^\circ, 30^\circ$ and 45° .

3.1.1. Water surface time series

Figs. 7 and 8 show η/h at relative distances $r/h = 5, 15, 25$ and 35 for Stokes and solitary waves (the other wave types are shown in Appendix A), respectively. Due to the smooth initiation for periodic waves, the $5T$ after the waves were fully developed are considered. Profiles for different θ are essentially identical at $r/h = 5$. However, differences in η/h increase with increasing r/h within the investigated domains.

The generated approximately linear waves propagated in deep water ($h/L = 0.50$) with weak non-linearity $H/h = 0.067$. At $r/h = 35$,

the ratio of H between geometries with $\theta = 45^\circ$ and $\theta = 0^\circ$ is 1.38. For Stokes waves with the same h as linear waves, $h/L = 0.39$ and the corresponding ratio of H is 1.36 (Fig. 7d). The cnoidal waves propagated in relatively shallower water depths with $h/L = 0.11$. Different θ resulted in varying degrees of wave steepening as the propagation distance increased from $r/h = 5$ to 35 , but the troughs remained almost unaffected. Fig. 8 shows η/h versus $t(g/h)^{1/2}$ for solitary waves. This steepening effect shows in increased H and faster wave propagation. In contrast to the diverging water body geometries examined in Ruffini et al. (2019), no trailing depression is observed across all geometries considered herein.

3.1.2. Wave height

Fig. 9 shows the relative wave heights H/h for linear, Stokes, cnoidal and solitary waves at all tested θ as a function of r/h , respectively. H for periodic waves is averaged over the $5T$ analysed in Section 3.1.1 for all H in this Section 3.1.2. For solitary waves, a is taken as the value of the crest of the leading wave. Fig. 9 clearly confirms the increasing wave steepening of H with θ for the results of all four wave types.

For geometries with curved wave sources, the wavefront length $l_w = b_0 - 2r\theta$ (Fig. 6) is used to link the H variation of idealised waves across water body geometries with different θ (Ruffini et al., 2019). In the idealised geometries with constant h , the term $(h_0/h)^{1/4}$ of Eq. (1) reduces to 1 and replacing b with l_w , results in

$$\frac{H}{H_0} = \left(\frac{l_{w0}}{l_w}\right)^{1/2} = (1 - L_w)^{-1/2}, \quad (11)$$

where $L_w = 1 - l_w/l_{w0}$ is the relative loss of l_w . Similarly, the equation for the 2/3 law by Xian-chu (1981) is

$$\frac{H}{H_0} = \left(\frac{l_{w0}}{l_w}\right)^{2/3} = (1 - L_w)^{-2/3}. \quad (12)$$

Fig. 10 illustrates that H/H_0 increases as l_w reduces (a/a_0 versus L_w are shown in Fig. A.3). For a better comparison with the theories of Green (1838) (Eq. (11)) and Xian-chu (1981) (Eq. (12)), all four wave types and investigated θ are related as H/H_0 versus L_w . H_0 is the wave height measured at the corresponding position in a 2D flume. The overall trend agrees with Eqs. (11) and (12), but there is a noticeable discrepancy as almost all points of cnoidal and solitary waves lie above the prediction from Eq. (11) and towards predictions from Eq. (12) due to the effect of wave non-linearity. Specifically, for $\theta = 7.5^\circ$ and 15° , the variation of H/H_0 is more gradual and closely follows Eq. (12). Conversely, for steeper angles ($\theta = 30^\circ$ and 45°), H/H_0 initially follows Eq. (11) and gradually approaches Eq. (12) with increasing L_w .

3.2. Straight wave source

This section starts with a theoretical analysis of the solitary wave propagation in converging water body geometries with a straight wave source, considering various wave conditions. The theoretical equations are introduced in Section 3.2.1 following the theory of Miles (1977b) for weakly non-linear waves and small oblique angles (small a/h and ψ). These main limitations are overcome in Section 3.2.2 by numerically investigating the effect of ψ for a range of a/h resulting in a new empirical equation for ψ_w . The effect of the water body width is then analysed in Section 3.2.3 which, in combination with findings in Section 3.2.2, results in a new prediction method for the wave amplification $\alpha = a/a_0$ along the sidewalls in converging water body geometries for a range of $a/h, b/h$ and θ .

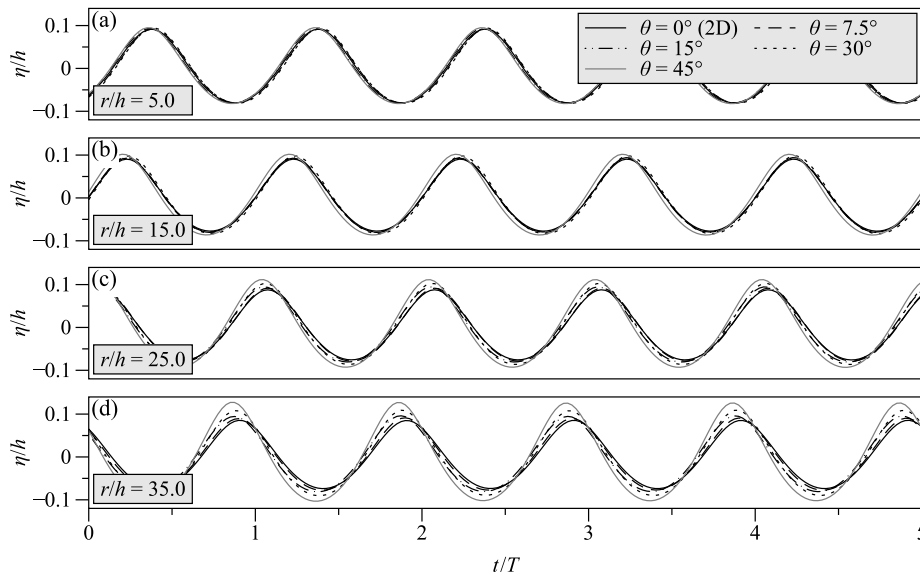


Fig. 7. Relative water surface elevation η/h versus time normalised with the wave period t/T for Stokes waves in all geometries with the curved wave source at different relative distances r/h .

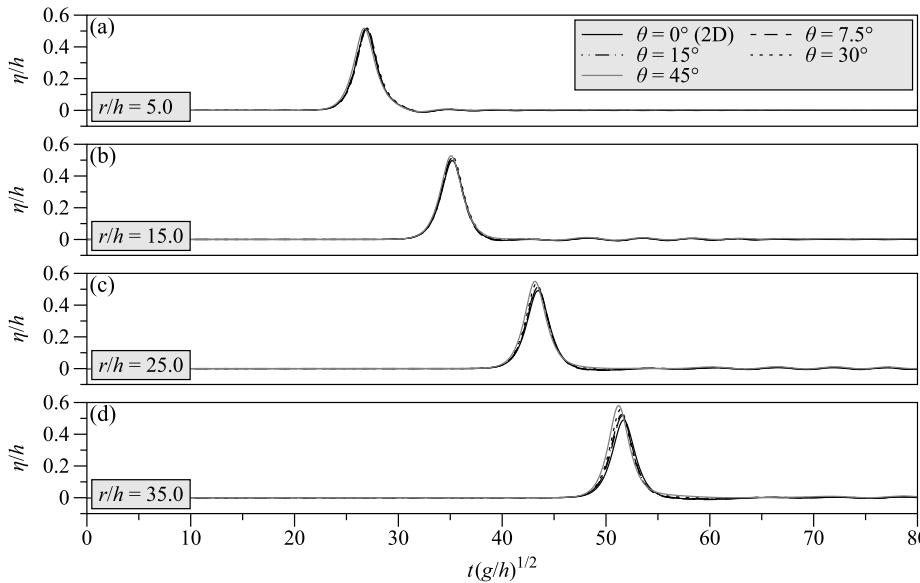


Fig. 8. Relative water surface elevation η/h versus normalised time $t(g/h)^{1/2}$ for solitary waves in all geometries with the curved wave source at different relative distances r/h .

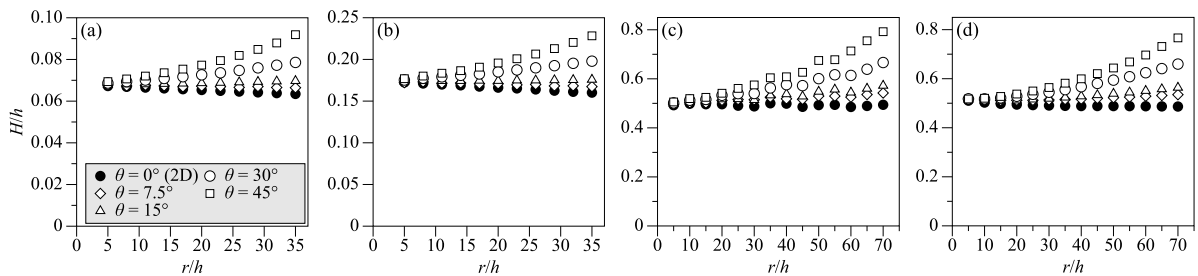


Fig. 9. Relative wave height variation with relative distance r/h for the (a) linear, (b) Stokes, (c) cnoidal and (d) solitary waves in all converging water body geometries with curved wave sources.

3.2.1. Theoretical considerations

The propagation of solitary waves in a geometry with a straight wave source is analysed theoretically. In contrast to a curved wave source, incident waves from straight wave sources impinge on sidewalls

with ψ and generate reflections. To simplify the analysis and avoid complications arising from the superposition and interaction between incident and reflected waves, solitary waves are used in the following study to represent the leading wave of a tsunami.

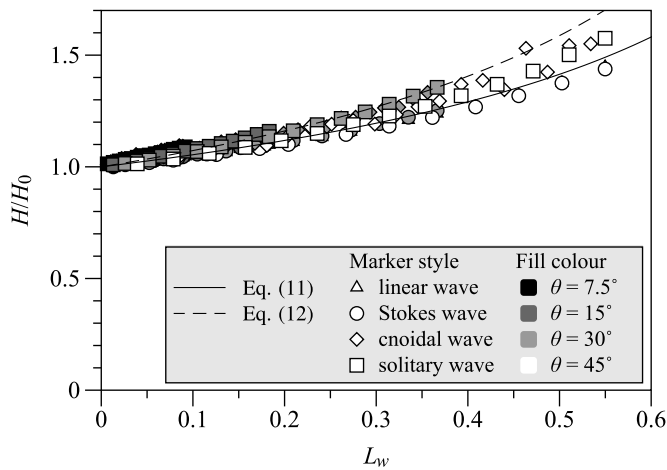


Fig. 10. Normalised wave height H/H_0 versus the relative loss of wavefront width L_w for all four wave types and investigated θ with curved wave sources.

Two cases can be distinguished based on ψ , giving rise to different reflection patterns introduced in Section 1. For large ψ , e.g. $\psi = 45^\circ$ for $a/h = 0.53$ ($K > 1$), regular reflection occurs when the incident solitary wave impinges on the wall, resulting in a linear reduction in the wavefront length as the geometry converges. Except for the stable stem at the wall, the characteristics of the incident wave should remain unchanged. However, for smaller ψ , Mach reflection occurs and the front of the incident waves locally rotates to match the wall boundary condition. This rotated front generates the so-called stem wave, which grows along the sidewall (Perroud, 1957; Miles, 1977b; Tanaka, 1993; Li et al., 2011). For the idealised geometry, assuming that ψ satisfies the condition to trigger Mach reflection for a given solitary wave and the converging water body is sufficiently long and wide, the transition slope from the stem wave to the incident wave can be ignored compared to l_s and the stem wave can be amplified to approach its asymptotic value (see Section 1).

The evolution of a solitary wave, propagating in an idealised geometry that satisfies aforementioned conditions, is shown in Fig. 11. As the solitary wave propagates, the growing stem waves from the two sides meet on the axis of symmetry and interact, resulting in a new wave system (one symmetric half of the wave system is shown in the upper half of Fig. 11). The location of the intersection point, where two stem waves meet, is defined as x' . Note that the oblique interaction of two identical solitons is equivalent to the interaction of one soliton with an oblique frictionless wall (Fig. 2, Miles, 1977b). The former stem wave becomes the new incident wave for the subsequent interaction stage. Note that the stem wave is still essentially a solitary wave (Li et al., 2011). The value of K decreases for the amplified new incident wave, leading to the interaction of the new incident wave still satisfying Mach reflection. This process is iterated until wave breaking occurs. The approximation of SWASH on wave breaking may underestimate the energy dissipation (Section 2.3), as the computation of phase velocity at the front face of the breaking wave could be inaccurate. Furthermore, due to the lack of theoretical modelling for wave breaking in Mach reflection, the present study did not analyse the post-breaking wave propagation. In the lower half of Fig. 11, the stem wave growth at different stages is represented by different shades of grey. Each stage is defined as an interaction that generates corresponding stem waves, with the subscript m indicating the stage number (positive integer).

Following the description of this iterative process, assuming that the wave is weakly non-linear and ψ is sufficiently small ($\sin \psi \approx \psi$), allows for the predictions of α_w and ψ_w using the theory of Miles (1977b) (Eqs. (3) and (4)) until $K_m \rightarrow 0$ ($\alpha_w \rightarrow 1$) or the wave breaking limit is reached, according to the criterion stated in Section 2.3. A non-dimensional parameter B_{lm} is introduced as the relative loss of water

body width, defined as $B_{lm} = 1 - b_m/b_{m-1}$. The equations for B_{lm} of interaction at sidewalls (odd stage) and interaction at $y/h = 0$ (even stage) are given by

$$B_{lm} = \begin{cases} \frac{\tan \psi \cdot \cot(\psi + \psi_{w_m}) + \tan^2 \psi}{1 + \tan^2 \psi} & \text{for } m = 2i - 1, \\ \frac{\tan \psi - \tan^2 \psi \cdot \tan \psi_{w_m}}{\tan \psi_{w_m} + \tan \psi} & \text{for } m = 2i, \end{cases} \quad (13)$$

where i is a positive integer. For a detailed derivation, see Appendix B. Note that b_m is a function of the abscissa (x_m) of the stem wave at the sidewall, which is the most important location in an engineering context (corresponding equations based on $y/h = 0$ are shown in Appendix B). To calculate B_{lm} , the equation for ψ_{w_m} in a given stage m can be obtained by substituting the corresponding K_m into Eq. (4), resulting in

$$\psi_{w_m} = \sqrt{\frac{a'_{m-1}}{3h} (1 - K_m)}, \quad (14)$$

where a'_{m-1} is a at the end of the stage $m - 1$. Meanwhile, a'_m can be obtained by the prediction of α_{w_m} , given as

$$\alpha_{w_m} = \frac{a'_m}{a'_{m-1}} = (1 + K_m)^2. \quad (15)$$

Thus far, the intersection point can be theoretically calculated to locate each stage and the upper limit of the corresponding a' is predictable. However, with the amplification at stages, the resulting wave eventually reaches a large a/h where the theory of Miles (1977b) becomes ineffective. This may result in a significant deviation between the theoretical model and the actual results (Tanaka, 1993; Li et al., 2011). Furthermore, for the investigated case with large $a/h = 0.53$ and $\psi = 30^\circ$, the deviation cannot be ignored even at the first stage. To address the limitation of the analytical solution, additional simulations are conducted for varying a/h and θ .

3.2.2. Effect of side angle

Due to a non-uniform wave profile over the y -direction generated by reflection, the Green's law (Eq. (11)) is not applicable in most positions, especially for relatively wide geometries. To investigate this, the converging water body with $b_0 = 60$ m, which is $200h$ for solitary waves, is simulated first. The snapshots and crest envelope contours for geometries with different θ are presented in Fig. 12. After 6 m propagation from the straight wave source, the measured $a/h = 0.493$ at $x/h = 0$, where the water body starts to converge.

The instantaneous snapshot contours in Fig. 12a-d show that a_r clearly increases from $\theta = 7.5^\circ$ to 45° . For the geometry with $\theta = 45^\circ$ ($K_{KY} = 1.35 > 1$) the wave system exhibits regular reflection, consistently with the theories of Miles (1977b) and Kodama and Yeh (2016). As expected, l_s barely grows with $\psi_w \approx 0$ at this value of ψ (identical to θ herein). For the remaining cases, l_s increases as the wave propagates (Fig. 12a-c), attributed to Mach reflection ($K_{KY} = 0.638$ for $\psi = 30^\circ$). Since $\alpha_r < 1$, the evolution of the wavefront for the incidence and the amplified stem is more important in tsunami hazard assessment. To facilitate the analysis of the crest envelope, Fig. 12e-h shows η_{max}/h , defined as the relative maximum water surface elevation during the propagation of the solitary wave in the water body. The stem wave boundary grows approximately linearly along the sidewall for geometries with $\theta = 7.5^\circ, 15^\circ$ and 30° . In the case of $\theta = 30^\circ$ ($K_{KY} = 0.638$), the stem wave first breaks at $x/h = 28$, then rapidly grows and breaks again at $x/h = 41$. While wave breaking causes significant reduction of H , it appears that it is confined to the wall region where the stem waves are higher. However, due to the SWASH approximation on wave breaking (Section 2.3) and lack of validation on stem wave breaking, the following analysis and discussion only apply to waves without or before breaking.

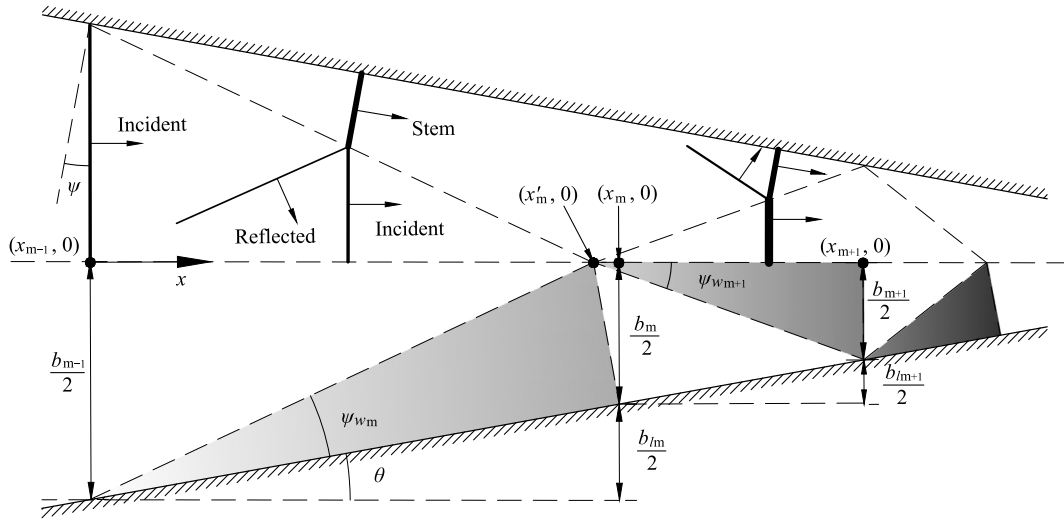


Fig. 11. Schematic view of a solitary wave propagation in an idealised converging geometry. Upper half: wave systems at different stages. The widths of the lines representing the wave crests are indicative of the size of the wave amplitude. Lower half: stem wave growth for different stages represented by different shades of grey.

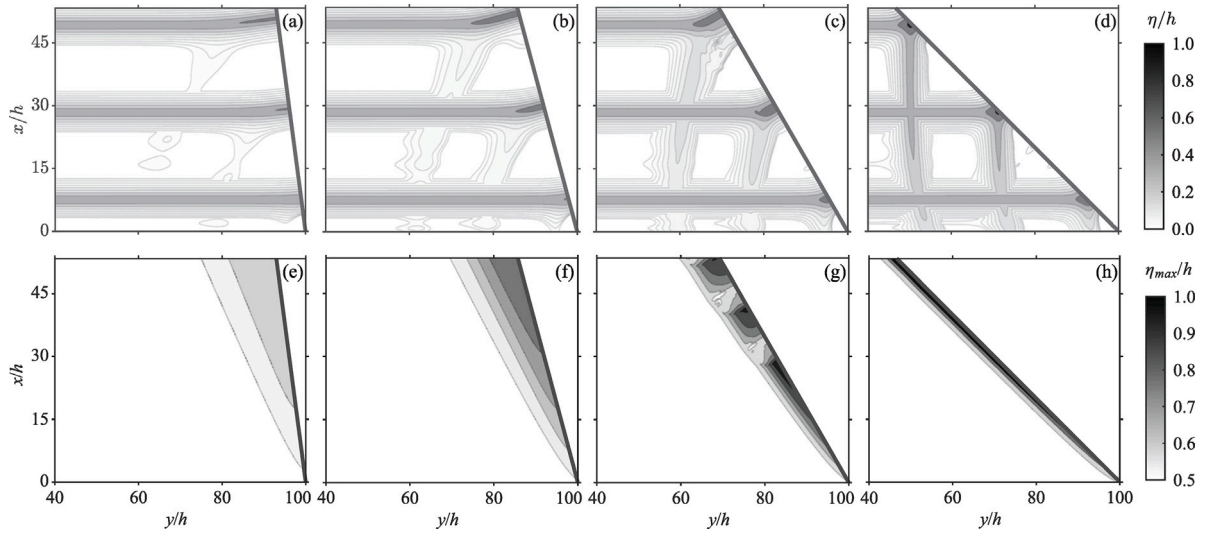


Fig. 12. Plan view of (a-d) η/h contour snapshots for every 3 s and (e-h) crest envelope contour for the solitary wave in geometries with $\theta = 7.5^\circ, 15^\circ, 30^\circ$ and 45° ($b_0/h = 200$).

The relative wave amplitudes a/h for solitary waves in the four geometries from Fig. 12 are shown in Fig. 13 along the sidewall and centre ($y/h = 0$) for $x/h \leq 50$. Within this range, a/h along $y/h = 0$ in geometries with different θ remain unaffected by the converging geometry. For the geometry with $\theta = 7.5^\circ$, the stem wave approaches its equilibrium $a/h = 0.640$ at $x/h = 50$. $\alpha_w = 1.28$ is slightly larger than 1.23 predicted by Eq. (3). However, for other geometries, due to K_{KY} being closer to the critical condition $K_{KY} = 1$, the distance to approach its equilibrium value is relatively larger, in line with the experiments of Li et al. (2011). Nevertheless, α_w in the geometry with $\theta = 15^\circ$ is 1.68 at $x/h = 50$, deviating 11% from the theoretical prediction of 1.51. This is in agreement with Tanaka (1993) for large a/h , as investigated in this study. The maximum stem wave height formed for $\theta = 30^\circ$ prior to the first time breaking is $a/h = 1.035$, exceeding the breaking criterion of a two-dimensional solitary wave $a/h = 0.827$ (Longuet-Higgins and Fenton, 1974) and stem wave $a/h = 0.910$ from Li et al. (2011).

ψ_w is calculated by $\tan \psi_w = l_s \cos \psi / x$ for each position of x , where l_s is the distance from the sidewall to the intersection point between the extension of the stem wave crest line perpendicular to the wall and the extension of the incident wave crest line (Fig. 2, Li et al., 2011). Finally, ψ_w is determined by performing linear regression on all measurements

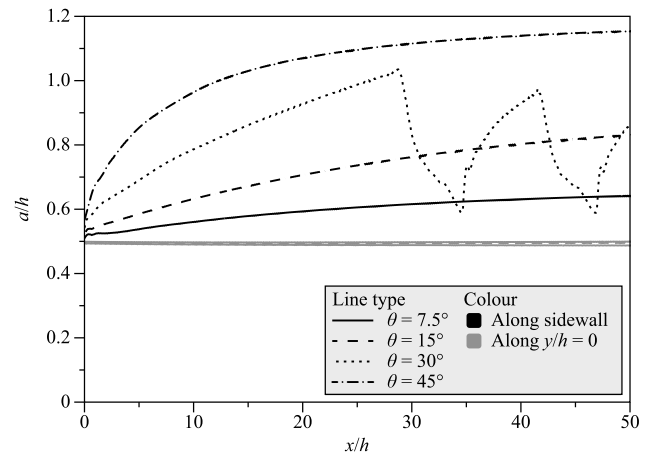


Fig. 13. Relative wave amplitude a/h variation with relative distance x/h for waves along the sidewall and $y/h = 0$ in geometries with different θ .

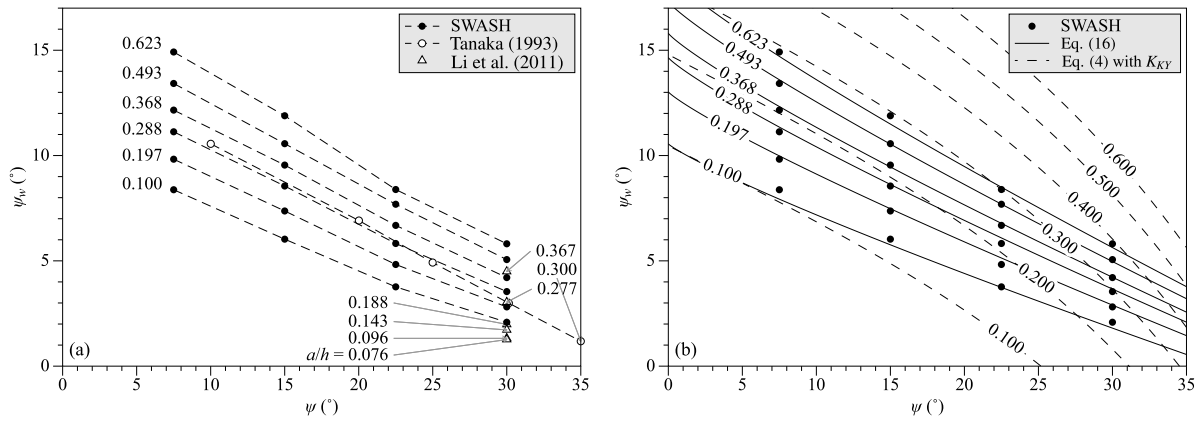


Fig. 14. ψ versus stem angle ψ_w with different a/h compared with (a) previous experiments and (b) analytical solution (Eq. (4)) and a new empirical equation (Eq. (16)).

Table 3
Fitting coefficients for Eq. (16).

Coefficient	Initial value	Fitting value	95% confidence interval
C_1	$1/\sqrt{3}$	0.376	(0.3457, 0.4063)
C_2	$1/2$	0.310	(0.2769, 0.3426)
C_3	$1/\sqrt{3}$	1.169	(1.065, 1.273)
C_4	$-1/2$	-0.0945	(-0.1268, -0.06219)
C_5	1	0.868	(0.7008, 1.034)

until the waves either reach the sponge layer or break. ψ_w is shown in Fig. 14a as a function of ψ for different a/h and the results are compared with Tanaka (1993) (numerical simulation) and Li et al. (2011) (laboratory experiment). The values decrease approximately linearly with ψ , consistently with the theory of Miles (1977b), and in agreement with the results of Tanaka (1993) and Li et al. (2011).

The analytical solution Eq. (4) is not effective in predicting ψ_w (Fig. 14b). As Tanaka (1993) concluded, large amplitude waves tend to significantly deviate in important parameters such as ψ_w and α_w . This still applies to the results of the laboratory experiments of Li et al. (2011) and present numerical results (Fig. 14). To address this issue, an empirical equation is developed by modifying Eq. (4) as a polynomial function of ψ and a/h of the form $\psi_w = C_1(a/h)^{C_2}[1 - C_3(a/h)^{C_4}\psi^{C_5}]$. To obtain the fitting coefficients C_1 to C_5 , the Trust-Region reflective algorithm for non-linear least squares fitting (a fitting function from the Curve fitting toolbox in Matlab 2022b) is used for the numerical results, with the coefficients in Eq. (4) as initial values. The Trust-Region reflective algorithm is a variation of the Trust-Region method, based on the interior-reflective Newton method, as described in Coleman and Li (1994, 1996). The empirical equation with the resulting coefficients (Table 3) is:

$$\psi_w = 0.376\left(\frac{a}{h}\right)^{0.310}\left[1 - 1.169\left(\frac{a}{h}\right)^{-0.0945}\psi^{0.868}\right]. \quad (16)$$

The normalised Root Mean Square Error (nRMSE), a measure of the prediction error relative to the range of the observed data (nRMSE = 0 represents perfect agreement), is used for testing Eq. (16),

$$\text{nRMSE} = \frac{\sqrt{\frac{1}{N} \sum_{i=1}^N (\hat{y}_i - \hat{y}_i)^2}}{\hat{y}_{\max} - \hat{y}_{\min}}, \quad (17)$$

where N is the number of data points, \hat{y} represents the observed values and \hat{y} denotes the predicted values. For the observed values from SWASH, Tanaka (1993) and Li et al. (2011), nRMSE = 0.0156, 0.046 and 0.162, respectively.

3.2.3. Effect of water body width

In contrast to the sidewall reflection in Fig. 12a ($b_0/h = 200$ and $\theta = 7.5^\circ$), reflection in a converging channel with $b_0/h = 5.3$ ($\theta = 5^\circ$)

for a single oblique sidewall was not observed in Wuppukondur and Baldock (2022). The main difference between the two cases is b_0/h . In order to study the influence of the water body width, b_0 is varied from $5h$ to $100h$. These numerical domains are designed to converge to 25% of b_0 ($B_l = 0.75$). More extreme values of B_l were excluded due to issues related to the aspect ratio of grids and excessive small time steps. In addition, the waves break in most cases for $a/h = 0.53$ with $B_l \geq 0.75$.

Fig. 15 shows water surface snapshots at different times and interval $0.1B_l$ for the geometry with $\theta = 7.5^\circ$ and $b_0/h = 50$. The narrower water body allows stem waves and transition slopes to reach $y/h = 0$ and superimpose. From the contour line of η/h at $B_l = 0.2$, slopes reaching the centre superimpose resulting in an increased η . With the increase of x/h , this effect intensifies, leading to a higher η observed at the centre compared to both sides. In addition to affecting the wavefront, the time interval to propagate 10% of b_0 keeps decreasing (Fig. 15). Note that B_l is based on the wavefront at $y/h = 0$ as the wavefront shapes change with B_l .

In Fig. 16, the η/h contour is shown in plan view for the geometry with $\theta = 7.5^\circ$ and $b_0/h = 100$, with snapshots taken every $0.05B_l$. Note that due to the rough contour lines selected, the small reflected waves (Fig. 12a) are not visible. However, the changing shape of the wavefront is clearly visible, with auxiliary dashed lines indicating the growth of the stem length during the first two stages, where the angles ψ_{w1} and ψ_{w2} are approximately 13.4° and 15.0° , respectively. In stage 3, wave breaking occurs at $B_l = 0.65$. As per the idealised case proposed in Section 3.2.1, new wave systems are generated either when the growing stem waves from both sides meet and interact at $y/h = 0$ (stage 2) or when the growing stem wave reaches the wall and interacts (stage 3).

Fig. 17 shows the wave crest in a half domain of the geometry with $\theta = 7.5^\circ$ and $b_0/h = 100$, with snapshots taken every $0.01B_l$ along the direction of wave propagation. Higher η_{\max}/h can be observed in the centre than at the sides for $0.34 < B_l < 0.56$. For $B_l > 0.56$, the crest is higher again at the sides than at the centre. Stem waves approaching their asymptotic state twice can clearly be observed for the first two stages. However, due to the transition slope from the stem wave to the incident wave, this process gradually changes from linear superposition of transition slope to non-linear interaction of stem waves. Therefore, to distinguish stages, a critical point is used, defined as where the wavefront has uniform η_{\max}/h , e.g. $B_l = 0.34$ and $B_l = 0.56$.

To further study the effect of stem wave growth on the wave crest spatial distribution, Fig. 18 shows contours of η_{\max}/H_0 in a half domain with $\theta = 7.5^\circ$ for $b_0/h = 5, 10, 20, 50$ and 100 from left to right ($\theta = 15^\circ$ and 30° are shown in Appendix C). For the geometry shown in Fig. 18a, which closely resembles the experimental conditions of Wuppukondur and Baldock (2022) ($\theta = 5^\circ$ and $b_0/h = 5.3$), minor reflections are observed and the cross-sections are almost uniform over the entire

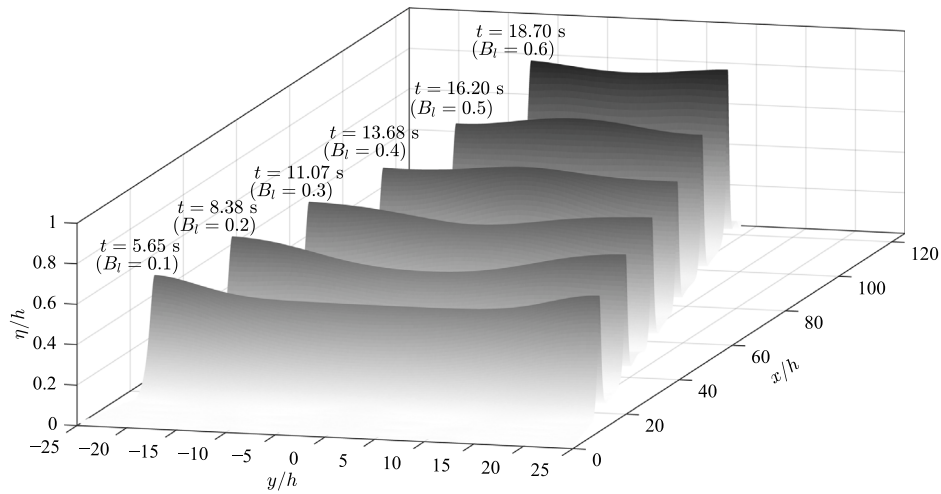


Fig. 15. Water surface snapshots of a solitary wave propagation in the geometry with $\theta = 7.5^\circ$ and $b_0/h = 50$ at different t with corresponding B_l .

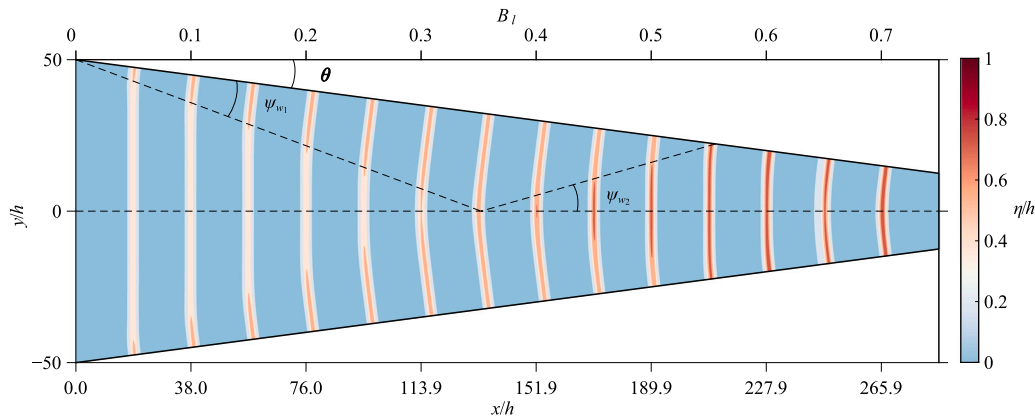


Fig. 16. Plan view of η/h contour snapshots for every $0.05B_l$ in the geometry with $\theta = 7.5^\circ$ and $b_0/h = 100$.

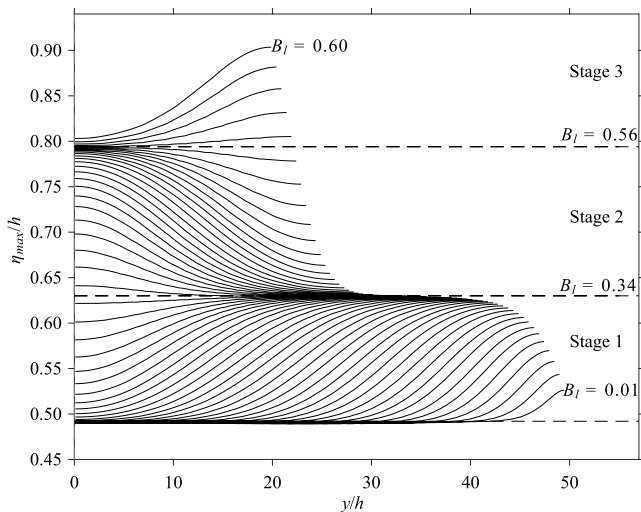


Fig. 17. Relative maximum water surface elevation η_{max}/h across the symmetrical half wavefront for solitary wave propagation in the geometry with $\theta = 7.5^\circ$ and $b_0/h = 100$ with snapshots taken every $0.01B_l$.

domain. It is apparent that the smaller θ and b_0/h , the more uniform the distribution becomes. Conversely, the distinct stages become clearer as wider water bodies have more space for stem wave growth. A

significant large wave can form when the stem waves with large α_w superimpose and interact. Therefore, wave breaking is more likely to occur in geometries with larger b_0/h for a given B_l .

The areas of large wave amplitude are of particular interest, occurring either at the sidewalls or at $y/h = 0$. Therefore, Fig. 19 shows α along the sidewall (dashed lines) and $y/h = 0$ (dotted lines) in geometries with different b_0/h (line colour) as a function of B_l compared with Green's law (solid black line). Lines stopped before $B_l = 0.7$ if wave breaking occurred, such as α in the geometries with $\theta = 7.5^\circ$ along the sidewall at $B_l = 0.65$ for $b_0/h = 50$ and $B_l = 0.62$ for $b_0/h = 100$ (Fig. 19a). After all, higher crests are hardly observed thereafter (Fig. 13). The maximum α prior to wave breaking is 1.87, 1.98 and 1.96 in cases where $\theta = 7.5^\circ, 15^\circ$ and 30° , respectively. As shown in Fig. 19c, when wave breaking occurs, waves along $y/h = 0$ are not yet increased by the stem wave interaction. More importantly, stem wave interaction and wave steepening can affect the maximum H and the wave-breaking positions. For $b_0/h = 5$ and 10 at $B_l = 0.6$ to 0.7 , the growth rates of α were significantly decreased (Fig. 19c). This is attributed to the fact that the converging water body starts from a wide (wave generation) to narrow section (wave absorption) such that the wavefront enters and leaves the converging water body ahead of the crest. In smaller b_0/h cases, L compared to l_0 becomes more significant, causing the wavefront to lose the constraint of the oblique walls before the crests reach the end of the converging water body.

Miles (1977b) theory only predicts the asymptotic value for wave amplification, however, the stem wave growth is also important for engineering applications. For geometries with $\theta = 7.5^\circ$ and 15° (Fig. 19a

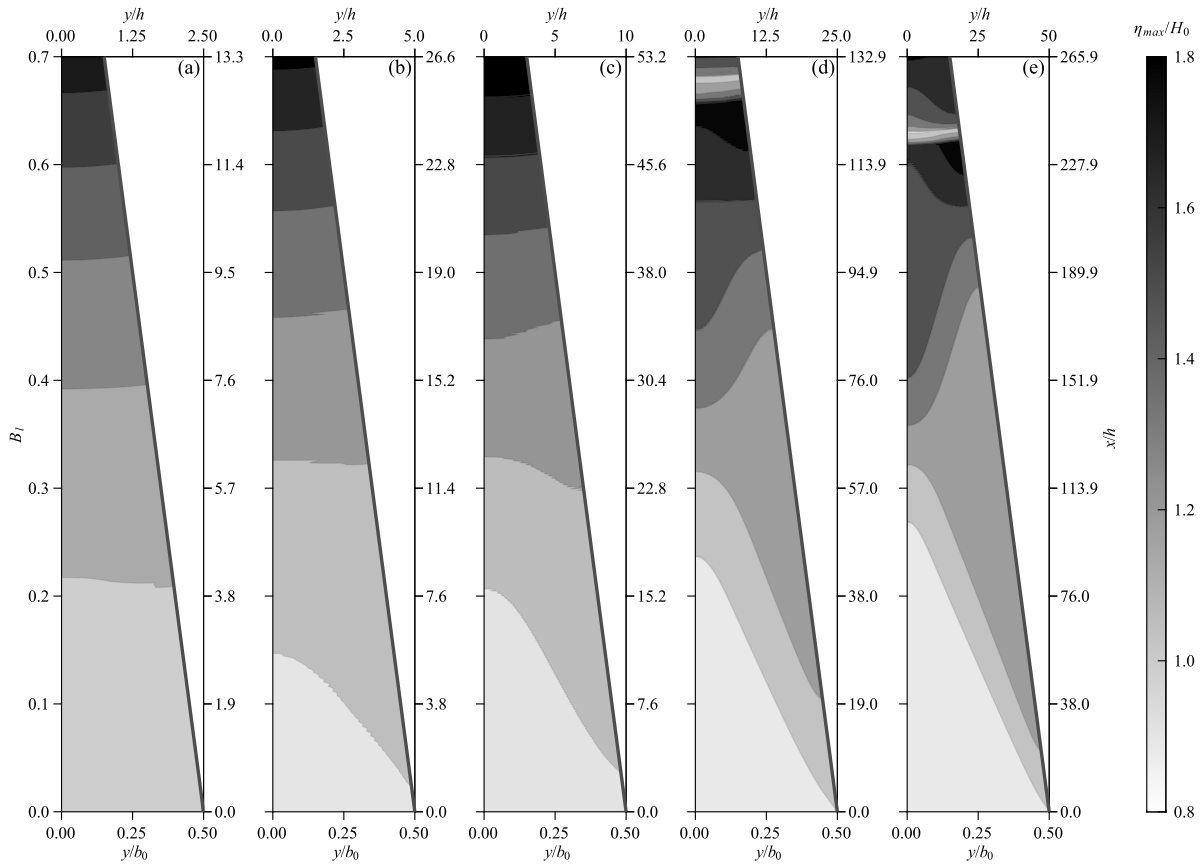


Fig. 18. Crest envelope contour for a solitary wave in geometries with $\theta = 7.5^\circ$ and (a) $b_0/h = 5$, (b) 10, (c) 20, (d) 50 and (e) 100.

and b), the maximum amplification between waves along the sidewall and $y/h = 0$ are $\alpha_w = 1.279$ ($b_0/h = 100$, $B_l = 0.195$) and $\alpha_w = 1.623$ ($b_0/h = 100$, $B_l = 0.397$). The maximum α_w becomes smaller and the crest envelope appears to approach Green's law better in geometries with smaller b_0/h . α and B_l substituted in Eq. (11) results in

$$\alpha = \left(\frac{b}{b_0}\right)^{-\frac{1}{2}} = (1 - B_l)^{-\frac{1}{2}}. \quad (18)$$

The maximum relative error between measurement and prediction of Eq. (18) for the wave along sidewalls is $\epsilon = 42\%$ in the geometry with $\theta = 30^\circ$ and $b_0/h = 100$. However, even when a is uniform across the wavefront, such as at the intersection point $B_l = 0.58$ for the geometry with $\theta = 15^\circ$ and $b_0/h = 100$, $\alpha = 1.66$ is still up to 8% larger than predicted by Greens law.

4. Discussion

4.1. Effect of the water body geometry

The effect of the water body geometry with a curved wave source on tsunami propagation is significant, with increasing θ leading to larger wave steepening for a given propagation distance. After removing the initial decay, weakly non-linear waves follow Green's law (Green, 1838, Eq. (11)) closely, while strongly non-linear waves (cnoidal and solitary) follow a $2/3$ law (Xian-chu, 1981, Eq. (12)) more closely (Fig. 10). For solitary waves generated by straight wave sources, not only θ , but also b_0/h significantly affect tsunami propagation. Comparing results for different b_0/h shows that a stem wave from Mach reflection in constrained converging water bodies requires a certain distance to approach the asymptotic value. As a result, for different water body widths, the available growth distance affects energy distribution during

solitary wave propagation (Fig. C.1). Hence, for geometries with $b_0/h = 5$, waves essentially follow the wave steepening law only without Mach reflection, as observed by Wuppukondur and Baldock (2022). In addition, the stem wave propagates 6%–14% faster than the solitary wave with the same amplitude (Li et al., 2011). Hence, the wave gradually becomes faster whilst the stem wave expands across the entire section of the converging water body.

4.2. Effect of the solitary wave amplitude on stem angle

Based on the theory of Miles (1977b), ψ_w depends on both ψ and a/h (Eq. (4)). However, for the investigated cases, the assumptions of weak non-linearity and small oblique angle cannot be ignored. Therefore, different a have been simulated and the corresponding ψ_w have been measured. The results were compared with numerical simulations of Tanaka (1993) and laboratory experiments of Li et al. (2011) in Fig. 14. Only some values for small a/h (e.g. $a/h < 0.2$) do not match well. The empirical Eq. (16) was fitted to the new results and used to predict the corresponding cases in Tanaka (1993) and Li et al. (2011). The accuracy of the prediction was assessed using nRMSE to provide an overall indication of reliability. Eq. (16) can successfully be used to overcome the limitation of the theory of Miles (1977b) in predicting ψ_w , particularly for large ψ and a/h within the investigation range.

4.3. Prediction method

For curved wave fronts at the entrance of a bay, channel or estuary, Green's law (Eq. (11)) can be used to predict linear and weakly non-linear waves. However, for strong non-linear cnoidal and solitary waves, Eq. (12) is more appropriate and conservative. For straight wave sources, existing theories do not cover $a/h > 0.1$. Therefore, a new

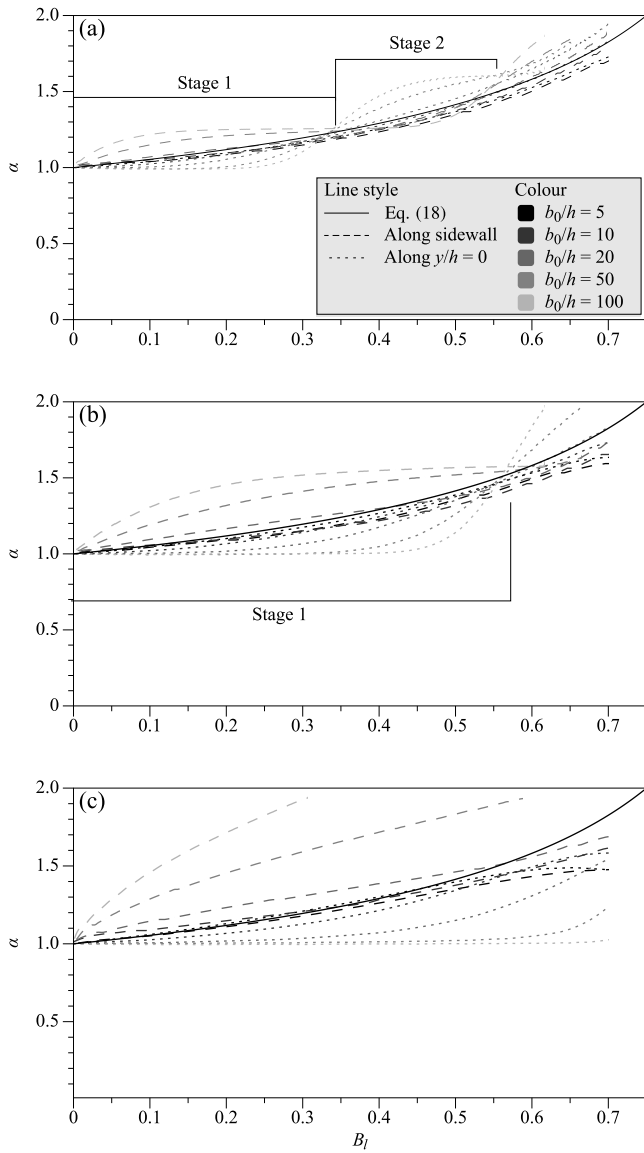


Fig. 19. Wave amplification α versus the relative loss of water body width B_l for solitary waves in geometries with different b_0/h and (a) $\theta = 7.5^\circ$, (b) 15° and (c) 30° .

method to predict a for solitary waves in converging geometries is proposed herein. Eq. (2) is used to obtain α for large b_0/h (e.g. $b_0/h > 10$). Substituting L_w with B_l in Eq. (2) yields

$$\alpha = \left(\frac{b}{b_0}\right)^{-\frac{2}{3}} = (1 - B_l)^{-\frac{2}{3}}. \quad (19)$$

The wave amplitude a'_m at the end of the stage m can be calculated with Eq. (19), given as

$$\alpha'_m = \left(\frac{b_m}{b_0}\right)^{-\frac{2}{3}} = \prod_{i=1}^m (1 - B_{l_i})^{-\frac{2}{3}}. \quad (20)$$

Considering the wave along the sidewall, a'_m calculated from Eq. (20) can be used to cover the corresponding stages of interaction at the wall and α from Eq. (19) can be used for the stages of interaction at $y/h = 0$, written as

$$\alpha_{(b_{m-1} < b \leq b_m)} = \begin{cases} \alpha'_m & \text{for } m = 2i - 1, \\ \left(\frac{b}{b_0}\right)^{-\frac{2}{3}} & \text{for } m = 2i. \end{cases} \quad (21)$$

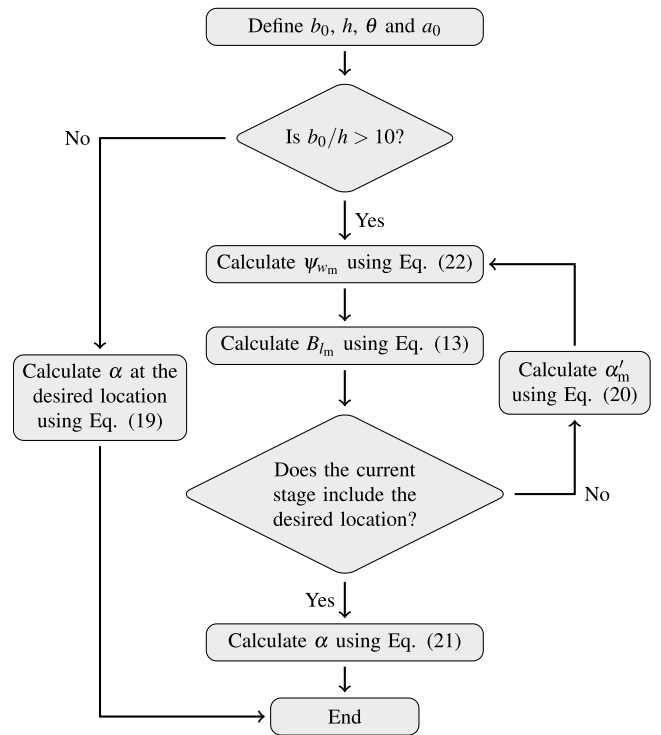


Fig. 20. Flow chart of the new prediction method for solitary wave propagation in converging geometries.

An equation for predicting ψ_{w_m} can be obtained by replacing a with a_m in Eq. (16), which can be further simplified to

$$\psi_{w_m} = 0.376\left(\frac{a_{m-1}}{h}\right)^{0.310} - 0.440\left(\frac{a_{m-1}}{h}\right)^{0.215} \psi^{0.868}. \quad (22)$$

The theory of Miles (1977b) is limited to the asymptotic state and assumptions whilst stem wave growth is more difficult to predict (Li et al., 2011). The proposed method avoids assessing the difference between the measured stem wave and its asymptotic value when propagating in a relatively wide water body. In addition, the strong non-linearity due to large a/h cause the asymptotic value to deviate from the prediction of Miles (1977b). Eq. (20) is therefore applied to a given wavefront with uniform a . A flow chart illustrating this method without considering wave breaking is shown in Fig. 20.

Throughout the process, calculations can be performed using dimensionless parameters such as a/h , b/h and θ , enabling the application of the method to different scales. Note that this method specifically addresses the propagation of solitary waves in relatively long water bodies, while not taking into account tsunami resonance and interaction with shoreline boundaries, which can also significantly contribute to tsunami amplification (Bellotti et al., 2012; Cortés et al., 2017). An example to illustrate this approach is inspired by the 2018 Palu Bay tsunami event. Inside Palu Bay, an average depth of 100 m is used as reference (Heidarzadeh et al., 2019). Note that Heidarzadeh et al. (2019) used a parabolic cross-section in their simulation. However, the varying bathymetry is not taken into consideration in this study. Instead, an idealised domain with a simplified geometry and flat bottom is employed. As shown in Fig. 1, $\theta = 7.5^\circ$ and $b = 9.4$ km to 5 km lead to $b_0/h = 94$ and $B_l = 0.47$, indicating a wide and long water body.

The 2018 Palu Bay event involved a complex wave pattern through a combination of seismic-generated and landslide-generated tsunamis originating from various locations along Palu Bay (Aránguiz et al., 2020). Here, however, the incident tsunami is simply modelled as a solitary wave with $a_0/h = 0.493$ and an idealised incident direction along the axis of symmetry. Note that the chosen a_0/h does not directly

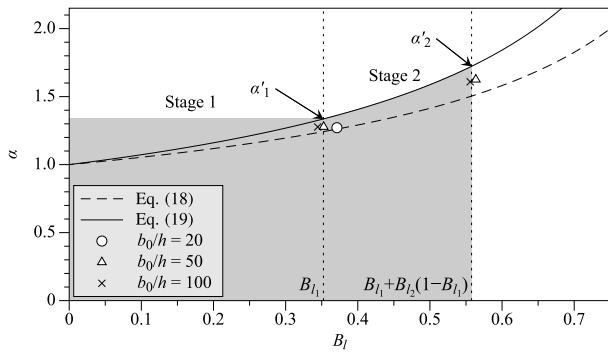


Fig. 21. Computation example of wave amplification α for a geometry with $\theta = 7.5^\circ$ compared with the results of SWASH.

represent the observed tsunami amplitude at Pantoloan tidal gauge ($a/h = 0.318$, Pakoksung et al., 2019; Pudjaprasetya et al., 2021). However, by using a slightly larger wave amplitude and vertical sidewalls, we can examine the tsunami's behaviour under idealised conditions. Note further that reflections at the end of the water body and resonance may be important when considering long tsunamis generated by seismic sources. Further studies are necessary to investigate the effect of incident wave direction and non-uniform bathymetry on tsunami propagation in order to fully predict less idealised cases such as the 2018 Palu Bay event.

The calculation of the idealised case is performed following the algorithm in Fig. 20. The stem angle for stage 1 using Eq. (22) is $\psi_{w_1} = 0.376 \times (0.493)^{0.310} - 0.440 \times (0.493)^{0.215} \times 0.131^{0.868} = 0.237$. Substituting ψ_{w_1} in Eq. (13) allows for the location of the end of stage 1 to be determined, resulting in a relative loss of water body width of $B_{l_1} = [\tan(0.131) \cot(0.131 + 0.237) + \tan^2(0.131)]/[1 + \tan^2(0.131)] = 0.35$. The predicted wave amplification is calculated with Eq. (21), yielding $\alpha_{(b_0 < b \leq b_1)} = \alpha'_1 = (1 - 0.35)^{-2/3} = 1.34$, as shown in the shaded area of Fig. 21. α' from present numerical results (Fig. 19a) are compared for different b_0/h . The predicted position of the end of stage 1 lies between the intersection point of the simulation cases with $b_0/h = 20$ and $b_0/h = 50$. Notably, the values of a along the sidewall and $y/h = 0$ are nearly uniform after the first intersection for the case with $b_0/h = 20$. The simulated α'_1 for all cases fall between the prediction of Eqs. (18) and (19).

Due to $B_{l_1} = 0.35 < 0.47$, the calculations continue for stage 2 by substituting a_1 into Eq. (22) resulting in $\psi_{w_2} = 0.376 \times (0.493 \times 1.34)^{0.310} - 0.440 \times (0.493 \times 1.34)^{0.215} \times 0.131^{0.868} = 0.262$. The location of the end of stage 2 can be determined by substituting ψ_{w_2} in Eq. (13), resulting in $B_{l_2} = [\tan(0.131) - \tan^2(0.131) \tan(0.262)]/[\tan(0.262) + \tan(0.131)] = 0.32$. Note that B_{l_2} is relative to b_1 , hence it is equal to $B_{l_1} + B_{l_2}(1 - B_{l_1}) = 0.56$ for b_0 . For this even stage, the predicted a is a function of B_l from Eq. (21), yielding $\alpha_{(b_1 < b \leq b_2)} = (b/b_0)^{-2/3} = (1 - B_l)^{-2/3}$ and $0.35 < B_l \leq 0.56$. Furthermore, $\alpha'_2 = \alpha_{(B_l=0.56)} = (1 - 0.56)^{-2/3} = 1.72$.

Thus far, different expressions have been applied to calculate a along the sidewall at different stages (interaction at the wall and $y/h = 0$). α'_1 and α'_2 are 5.85% and 8.55% greater than the simulated values of the case with $b_0/h = 50$, respectively, which tend to work on the safe side. This method could also be applicable to curved wave sources with $0 < \lambda < 2\theta/b_0$. However, the method becomes increasingly conservative with increasing λ .

5. Conclusions

In this study, the effect of the converging water body geometry on tsunami propagation was investigated numerically. The study focused on idealised converging, uniform-depth water bodies with oblique side walls with varying side angles θ . Both curved and straight

wave sources were investigated to exclude or take sidewall reflection into account, respectively. The non-hydrostatic non-linear shallow water model SWASH was used. This was validated with numerical simulations (Tanaka, 1993), laboratory experiments (Li et al., 2011) and analytical solutions (Green, 1838; Xian-chu, 1981), with a focus on wave steepening.

For curved wave sources, the distribution of approximately linear, Stokes, cnoidal and solitary waves was analysed for geometries with different $\theta = 0^\circ$ (2D), 7.5° , 15° , 30° and 45° . The time series of the normalised water surface elevation η/h profiles were compared at values of relative distance from $r/h = 5$ to 35 with the water depth h . Furthermore, the analysis of wave characteristics, such as wave steepening, was presented, where the normalised wave height H/h increased non-linearly with increasing θ . The relative loss of the wavefront length L_w was introduced and the comparison of these geometries using the equations based on Green's law (Eq. (11)) and Xian-chu (1981) (Eq. (12)) was presented. The overall propagation of linear and Stokes waves agreed with the prediction of Eq. (11). However, for cnoidal and solitary waves, most results were closer to Eq. (12) than Eq. (11).

For straight wave sources, tsunamis propagating along the axis of symmetry impact the sidewalls at an oblique angle ψ , which has the same value as θ . The wave field is not uniform across the water body geometry. The propagation of solitary waves in a sufficiently long and wide converging water body were first discussed theoretically. Under the approximations of the Miles (1977b) theory (weak non-linearity and small oblique angle), theoretical multiple-stage equations were derived to predict the stem angle ψ_w (Eq. (14)) and the stem wave amplification α_w for each 'stage', where a new wave system was generated from stem waves interaction. Furthermore, simulations were conducted for a straight wave source to compare the results of ψ_w with theory and experimental results, particularly in scenarios involving large angles ($\theta = 7.5^\circ$, 15° , 22.5° and 30°) and amplitudes ($a/h = 0.1$ to 0.623). The obtained ψ_w agreed with those of Tanaka (1993) and Li et al. (2011), but significant deviations were observed when compared to the analytical solution (Miles, 1977b; Kodama and Yeh, 2016). Consequently, the empirical Eq. (16) was introduced to predict ψ_w . To study the effect of the water body width, additional simulations were conducted with the initial water body width b_0 from $5h$ to $100h$. It was observed that as θ and b_0/h decreased, a/h became more uniform across the water bodies. Conversely, wider water bodies provide more space for stem wave growth, resulting in distinct stages of new wave systems.

This work proposed a new prediction method for a of solitary waves in a converging water body, considering the identified multi-stage propagation for interaction at the wall and centre. An example, inspired by the 2018 Palu Bay event, illustrated this approach using $\theta = 7.5^\circ$ compared with the results of the SWASH simulation. Although errors can accumulate within a few stages before wave breaking occurs, the results indicated that the method is conservative and has potential for use in tsunami prediction and hazard assessment.

Future research will focus on modelling the propagation of tsunami-like waves in geometries involving non-uniform bathymetries. Including the effect of currents in wave height prediction tools is another potential avenue for improving predictions across a wider range of scenarios.

Notation

a	wave amplitude [L]
a'	amplified wave amplitude at the end of the corresponding stage [L]
a_r	reflected wave amplitude [L]
a_w	stem wave amplitude [L]
B_l	relative loss of water body width [-]
b	water body width [L]
C	fitting coefficient [-]

C_r	Courant number [-]
c	wave speed [LT^{-1}]
c_f	bottom friction coefficient [-]
d	total water depth [L]
g	gravitational acceleration [LT^{-2}]
H	wave height [L]
h	water depth [L]
K	interaction parameter of Miles (1977b) [-]
K_K	interaction parameter of Kodama et al. (2009) [-]
K_{KY}	interaction parameter of Kodama and Yeh (2016) [-]
k	wave number [L^{-1}]
L	wavelength [L]
L_w	relative loss of wavefront length [-]
l_0	converging water body length [L]
l_s	stem length [L]
l_w	wavefront length [L]
N	number of data points [-]
n	Manning's roughness coefficient [$\text{TL}^{-1/3}$]
p_t	total pressure [$\text{ML}^{-1}\text{T}^{-2}$]
q	non-hydrostatic pressure term [$\text{ML}^{-1}\text{T}^{-2}$]
r	radial distance [L]
T	wave period [T]
t	time from when the wave is generated [T]
u	velocity component in x direction [LT^{-1}]
\bar{u}	depth averaged velocity component in x direction [LT^{-1}]
v	velocity component in y direction [LT^{-1}]
\bar{v}	depth averaged velocity component in y direction [LT^{-1}]
x	x -coordinate [L]
x'	location where the offshore stem waves meet [L]
y	y -coordinate [L]
\hat{y}	observed value [-]
\hat{y}	predicted value [-]
z	z -coordinate [L]

Greek symbols

α	wave amplification [-]
α_r	reflected wave amplification [-]
α_w	stem wave amplification [-]
γ	wave propagation angle from the curved wave source [-]
Δt	time difference [T]
Δx	x -direction grid size [L]
Δy	y -direction grid size [L]
ϵ	relative error [-]
η	free water surface elevation [L]
θ	water body side angle [-]
λ	curvature of curved wave source [L^{-1}]
τ	turbulent stress [ML^3T^{-2}]
ψ	angle between incident wave and lateral wall [-]
ψ_r	reflected angle [-]
ψ_w	stem angle [-]

Subscripts

i	positive integer
m	stage number
max	maximum
min	minimum
0	initial or reference

Abbreviations

BDF	Backward Differentiation Formula
CDF	Central Differentiation Formula

CFL	Courant–Friedrichs–Lewy
CPU	Central Processing Unit
HPC	High Performance Computing
KP	Kadomtsev–Petviashvili
KdV	Korteweg–de Vries
MPI	Message Passing Interface
NLSWE	Non-Linear Shallow Water Equation
SPH	Smoothed Particle Hydrodynamics
nRMSE	normalised Root Mean Square Error
2D	Two-Dimensional

CRedit authorship contribution statement

Zhiwen Chen: Conceptualization, Methodology, Investigation, Funding acquisition, Formal analysis, Validation, Visualization, Writing – original draft, Writing – review & editing. **Valentin Heller:** Conceptualization, Methodology, Project administration, Supervision, Validation, Writing – review & editing. **Riccardo Briganti:** Conceptualization, Methodology, Supervision, Validation, Writing – review & editing.

Declaration of competing interest

The authors declare that they have no known competing financial interests or personal relationships that could have appeared to influence the work reported in this paper.

Data availability

Data will be made available on request.

Acknowledgements

The authors would like to thank Dr Gioele Ruffini for providing numerical results and helpful suggestions. The numerical simulations have been conducted on the University of Nottingham HPC clusters Augusta.

Appendix A

Figs. A.1 and A.2 show η/h at relative distances $r/h = 5, 15, 25$ and 35 for linear and cnoidal waves, respectively. Fig. A.3 shows a/a_0 as a function of L_w for all four wave types and the investigated θ , in comparison with the theories of Green (1838) and Xian-chu (1981).

For the wave amplitude, similar equations to Eqs. (11) and (12) can be obtained by using $H = 2a$

$$\frac{a}{a_0} = \left(\frac{l_{w0}}{l_w}\right)^{1/2} = (1 - L_w)^{-1/2}, \quad (\text{A.1})$$

$$\frac{a}{a_0} = \left(\frac{l_{w0}}{l_w}\right)^{2/3} = (1 - L_w)^{-2/3}. \quad (\text{A.2})$$

Appendix B

This appendix provides a detailed derivation of Eq. (13). Based on the notation shown in Fig. 11, for the interaction at the wall (odd stage m),

$$\begin{aligned} x_m - x_{m-1} &= \frac{b_{l_m}}{2 \tan \psi}, \\ x_m - x'_m &= \frac{b_m}{2} \tan \psi = \frac{(b_{m-1} - b_{l_m})}{2} \tan \psi, \\ x'_m - x_{m-1} &= \frac{b_{m-1}}{2} \cot(\psi + \psi_{w_m}). \end{aligned} \quad (\text{B.1})$$

Eq. (B.1) is substituted into $x_m - x_{m-1} = (x_m - x'_m) + (x'_m - x_{m-1})$ resulting in

$$\frac{b_{l_m}}{2 \tan \psi} = \left(\frac{b_{m-1}}{2} - \frac{b_{l_m}}{2}\right) \tan \psi + \frac{b_{m-1}}{2} \cot(\psi + \psi_{w_m}), \quad (\text{B.2})$$

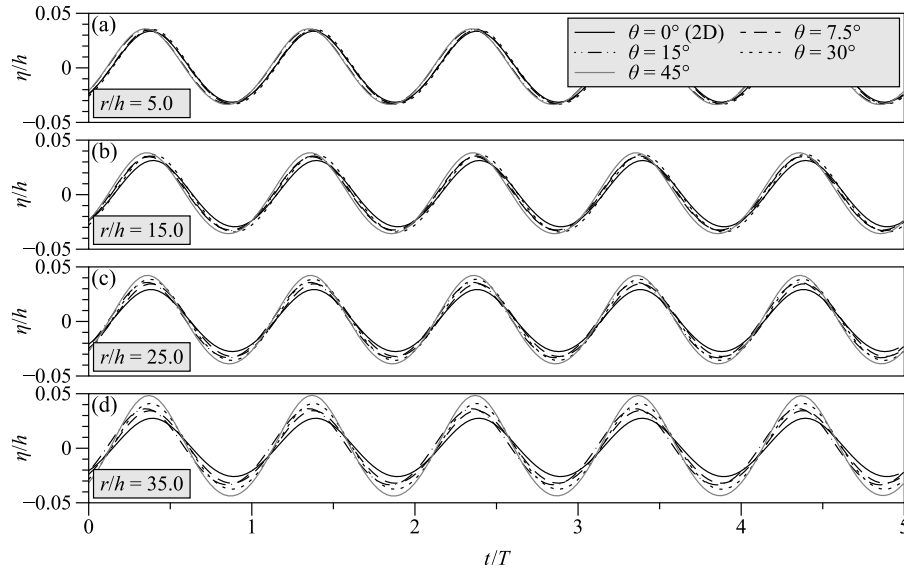


Fig. A.1. Relative water surface elevation η/h versus time normalised with the wave period t/T for approximate linear waves in all geometries with the curved wave source at different relative distances r/h .

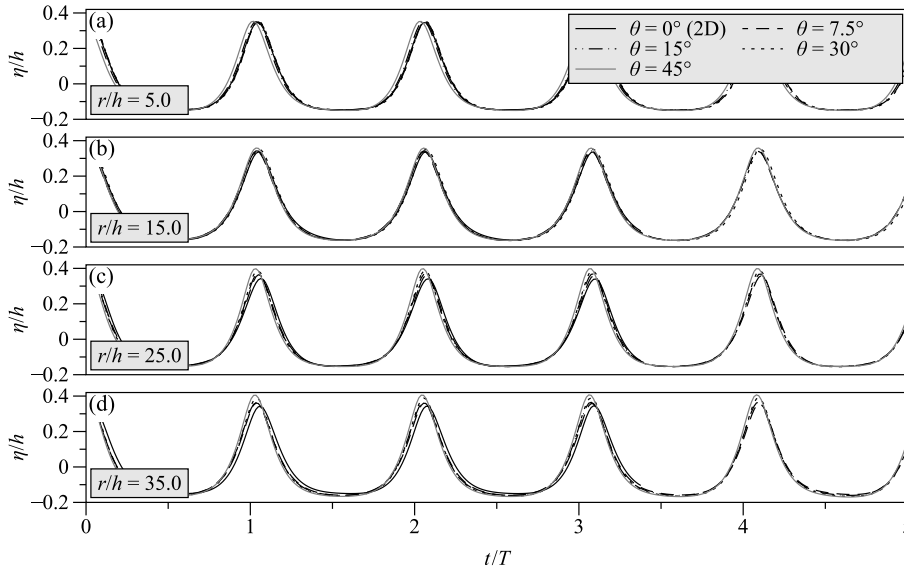


Fig. A.2. Relative water surface elevation η/h versus time normalised with the wave period t/T for cnoidal waves in all geometries with the curved wave source at different relative distances r/h .

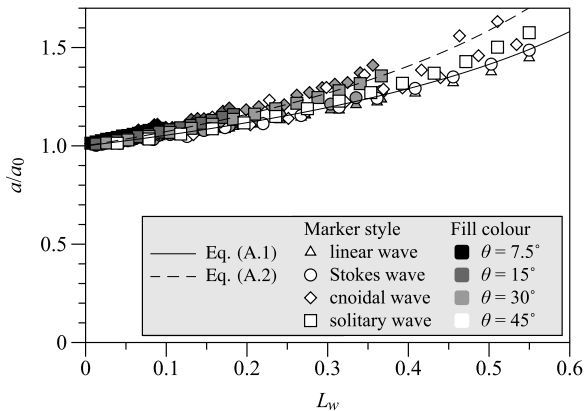


Fig. A.3. Normalised wave amplitude a/a_0 versus the relative loss of water body width L_w for all four wave types and investigated θ .

yielding

$$b_{l_m} (1 + \tan^2 \psi) = b_{m-1} [\tan \psi \cdot \cot(\psi + \psi_{w_m}) + \tan^2 \psi]. \quad (\text{B.3})$$

The equation for B_{l_m} is then given by

$$B_{l_m} = \frac{b_{l_m}}{b_{m-1}} = \frac{\tan \psi \cdot \cot(\psi + \psi_{w_m}) + \tan^2 \psi}{1 + \tan^2 \psi}. \quad (\text{B.4})$$

Similarly, for the interaction at $y/h = 0$ (even stage $m + 1$),

$$x_{m+1} - x'_m = \frac{b_{m+1}}{2 \tan \psi_{w_{m+1}}} = \frac{b_m - b_{l_{m+1}}}{2 \tan \psi_{w_{m+1}}},$$

$$x_{m+1} - x_m = \frac{b_{l_{m+1}}}{2 \tan \psi}, \quad (\text{B.5})$$

$$x_m - x'_m = \frac{b_m}{2} \tan \psi.$$

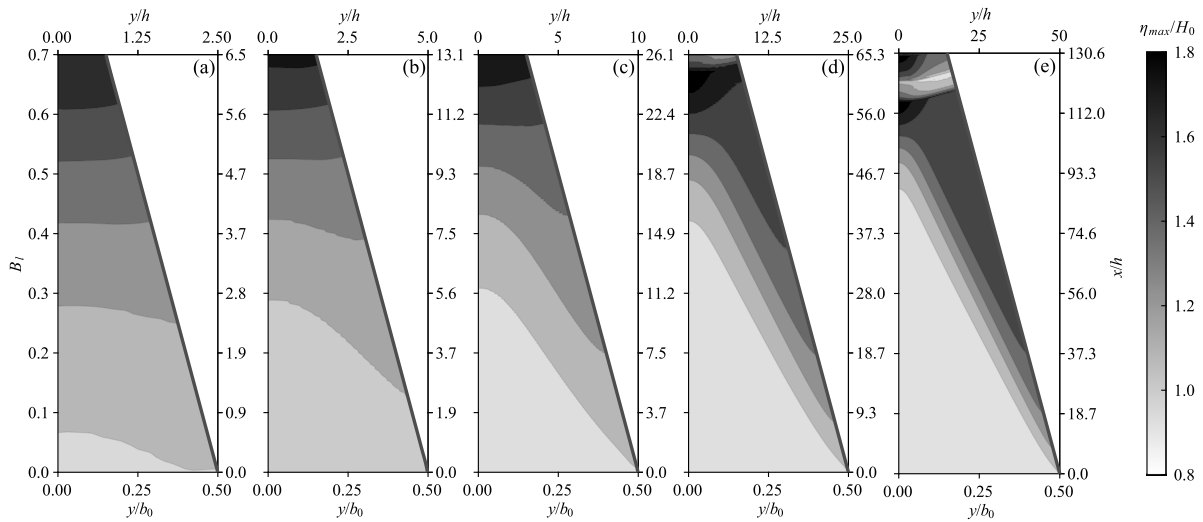


Fig. C.1. Crest envelope contour for a solitary wave in geometries with $\theta = 15^\circ$ and (a) $b_0/h = 5$, (b) 10, (c) 20, (d) 50 and (e) 100.

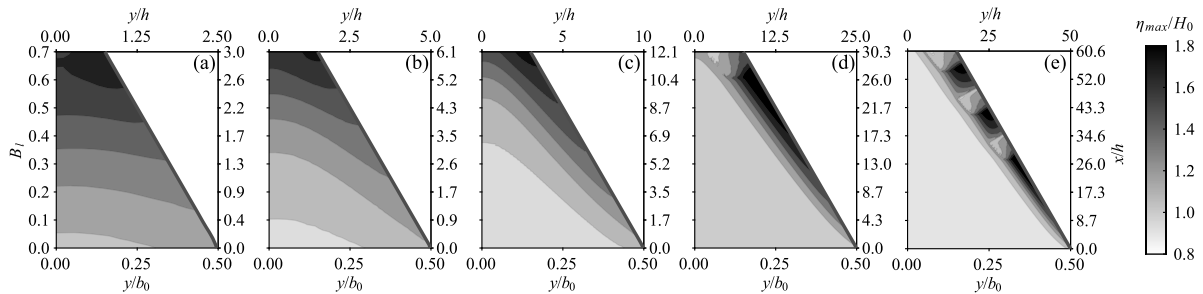


Fig. C.2. Crest envelope contour for a solitary wave in geometries with $\theta = 30^\circ$ and (a) $b_0/h = 5$, (b) 10, (c) 20, (d) 50 and (e) 100.

Eq. (B.5) is substituted into $x_{m+1} - x'_m = (x_{m+1} - x_m) + (x_m - x'_m)$ resulting in

$$\frac{b_m - b'_{m+1}}{2 \tan \psi_{w_{m+1}}} = \frac{b_{m+1}}{2 \tan \psi} + \frac{b_m}{2} \tan \psi, \quad (\text{B.6})$$

yielding

$$b_{m+1} (\tan \psi_{w_{m+1}} + \tan \psi) = b_m (\tan \psi - \tan^2 \psi \cdot \tan \psi_{w_{m+1}}). \quad (\text{B.7})$$

The equation for $B_{l_{m+1}}$ is then given by

$$B_{l_{m+1}} = \frac{b_{m+1}}{b_m} = \frac{\tan \psi - \tan^2 \psi \cdot \tan \psi_{w_{m+1}}}{\tan \psi_{w_{m+1}} + \tan \psi}. \quad (\text{B.8})$$

By considering the position of the stem wave at $y/h = 0$, the equations for calculating B_{l_m} can be obtained in the same manner, given by

$$B_{l_m} = \begin{cases} \tan \psi \cdot \cot(\psi + \psi_{w_m}) & \text{for } m = 2i - 1, \\ \frac{\tan \psi}{\tan \psi_{w_m} + \tan \psi} & \text{for } m = 2i. \end{cases} \quad (\text{B.9})$$

Appendix C

Figs. C.1 and C.2 show contours of η_{max}/H_0 in a half domain with $\theta = 15^\circ$ and 30° for $b_0/h = 5, 10, 20, 50$ and 100 from left to right.

References

Aránguiz, R., Esteban, M., Takagi, H., Mikami, T., Takabatake, T., Gómez, M., González, J., Shibayama, T., Okuwaki, R., Yagi, Y., Shimizu, K., Achiari, H., Stolle, J., Robertson, I., Ohira, K., Nakamura, R., Nishida, Y., Krautwald, C., Goseberg, N., Nistor, I., 2020. The 2018 Sulawesi tsunami in Palu City as a result of several landslides and coseismic tsunamis. *Coast. Eng. J.* 62, 445–459.

Bellotti, G., Briganti, R., Beltrami, G.M., Franco, L., 2012. Modal analysis of semi-enclosed basins. *Coast. Eng.* 64, 16–25.

Boussinesq, J., 1872. Théorie des ondes et des remous qui se propagent le long d'un canal rectangulaire horizontal, en communiquant au liquide contenu dans ce canal des vitesses sensiblement pareilles de la surface au fond. *J. Math. Pures Appl.* 2e série 17, 55–108.

Cecioni, C., Iorio, V., Bellotti, G., Grilli, S.T., 2023. Probabilistic landslide tsunami modeling of the 2018 Palu Bay event. *Coast. Eng.* 183, 104332.

Chang, P., Melville, W., Miles, J., 1979. On the evolution of a solitary wave in a gradually varying channel. *J. Fluid Mech.* 95, 401–414.

Chen, Z., Heller, V., Briganti, R., 2023. Numerical modelling of tsunami propagation in converging channels. In: 40th International Association for Hydro-Environmental Engineering and Research World Congress. IAHR.

Coleman, T.F., Li, Y., 1994. On the convergence of interior-reflective Newton methods for nonlinear minimization subject to bounds. *Math. Program.* 67, 189–224.

Coleman, T.F., Li, Y., 1996. An interior trust region approach for nonlinear minimization subject to bounds. *SIAM J. Optim.* 6, 418–445.

Cortés, P., Catalán, P.A., Aránguiz, R., Bellotti, G., 2017. Tsunami and shelf resonance on the northern Chile coast. *J. Geophys. Res.: Oceans* 122, 7364–7379.

Dean, R.G., Dalrymple, R.A., 1991. *Water Wave Mechanics for Engineers and Scientists*, vol. 2, World Scientific.

Evers, F.M., Heller, V., Fuchs, H., Hager, W.H., Boes, R., 2019. Landslide-generated impulse waves in reservoirs. In: Boes, R. (Ed.), *Basics and Computation*. In: VAW-Mitteilung, vol. 254, ETH Zurich, Zurich.

Fenton, J., 1985. A fifth-order Stokes theory for steady waves. *J. Waterw. Port Coast. Ocean Eng.* 111, 216–234.

Fenton, J.D., 1999. Chapter 2 - the cnoidal theory of water waves. In: Herbich, J.B., Ansari, K.A., Chakrabarti, S.K., Demirbilek, Z., Fenton, J.D., Isobe, M., Kim, M., Panchang, V.G., Randall, R.E., Triantafyllou, M.S., Webster, W.C., Xu, B. (Eds.), *Developments in Offshore Engineering*. Gulf Professional Publishing, Houston, pp. 55–100.

Franco, A., Schneider-Muntau, B., Roberts, N.J., Clague, J.J., Gems, B., 2021. Geometry-based preliminary quantification of landslide-induced impulse wave attenuation in mountain lakes. *Appl. Sci.* 11, 11614.

Fritz, H., Hager, W., Minor, H.-E., 2001. Lituya Bay case: Rockslide impact and wave run-up. *Sci. Tsunami Hazards* 19, 3–22.

- Gidel, F., Bokhove, O., Kalogirou, A., 2017. Variational modelling of extreme waves through oblique interaction of solitary waves: Application to Mach reflection. *Nonlinear Processes Geophys.* 24, 43–60.
- Goda, K., Mori, N., Yasuda, T., Prasetyo, A., Muhammad, A., Tsujio, D., 2019. Cascading geological hazards and risks of the 2018 Sulawesi Indonesia earthquake and sensitivity analysis of tsunami inundation simulations. *Front. Earth Sci.* 7, 261.
- Goring, D.G., 1979. *Tsunamis—The Propagation of Long Waves Onto a Shelf* (Ph.D. thesis). California Institute of Technology.
- Green, G., 1838. On the motion of waves in a variable canal of small depth and width. *Trans. Cambridge Philos. Soc.* 6, 457.
- Gylfadóttir, S.S., Kim, J., Helgason, J.K., Brynjólfsson, S., Höskuldsson, Á., Jóhannesson, T., Harbitz, C.B., Løvholt, F., 2017. The 2014 Lake Askja rockslide-induced tsunami: Optimization of numerical tsunami model using observed data. *J. Geophys. Res.: Oceans* 122, 4110–4122.
- Heidarzadeh, M., Muhari, A., Wijanarto, A.B., 2019. Insights on the source of the 28 September 2018 Sulawesi tsunami, Indonesia based on spectral analyses and numerical simulations. *Pure Appl. Geophys.* 176, 25–43.
- Heller, V., Brüggemann, M., Spinneken, J., Rogers, B.D., 2016. Composite modelling of subaerial landslide-tsunamis in different water body geometries and novel insight into slide and wave kinematics. *Coast. Eng.* 109, 20–41.
- Heller, V., Hager, W.H., 2010. Impulse product parameter in landslide generated impulse waves. *J. Waterw. Port Coast. Ocean Eng.* 136, 145–155.
- Heller, V., Hager, W.H., 2011. Wave types of landslide generated impulse waves. *Ocean Eng.* 38, 630–640.
- Heller, V., Moalemi, M., Kinnear, R., Adams, R., 2012. Geometrical effects on landslide-generated tsunamis. *J. Waterw. Port Coast. Ocean Eng.* 138, 286–298.
- Heller, V., Ruffini, G., 2023. A critical review about generic subaerial landslide-tsunami experiments and options for a needed step change. *Earth-Sci. Rev.* 242, 104459.
- Hilbe, M., Anselmetti, F.S., 2015. Mass movement-induced tsunami hazard on perialpine Lake Lucerne (Switzerland): Scenarios and numerical experiments. *Pure Appl. Geophys.* 172, 545–568.
- Knowles, J., Yeh, H., 2018. On shoaling of solitary waves. *J. Fluid Mech.* 848, 1073–1097.
- Knowles, J., Yeh, H., 2019. Fourfold amplification of solitary-wave Mach reflection at a vertical wall. *J. Fluid Mech.* 861, 517–523.
- Kodama, Y., Oikawa, M., Tsuji, H., 2009. Soliton solutions of the KP equation with V-shape initial waves. *J. Phys. A* 42, 312001.
- Kodama, Y., Yeh, H., 2016. The KP theory and Mach reflection. *J. Fluid Mech.* 800, 766–786.
- Krautwald, C., Stolle, J., Robertson, I., Achiari, H., Mikami, T., Nakamura, R., Takabatake, T., Nishida, Y., Shibayama, T., Esteban, M., Goseberg, N., Nistor, I., 2021. Engineering lessons from September 28, 2018 Indonesian tsunami: Scouring mechanisms and effects on infrastructure. *J. Waterw. Port Coast. Ocean Eng.* 147, 04020056.
- Lam, D., Simpson, R., 1976. Centered differencing and the box scheme for diffusion convection problems. *J. Comput. Phys.* 22, 486–500.
- Li, W., Yeh, H., Kodama, Y., 2011. On the Mach reflection of a solitary wave: Revisited. *J. Fluid Mech.* 672, 326–357.
- Longuet-Higgins, M.S., Fenton, J., 1974. On the mass, momentum, energy and circulation of a solitary wave. II. *Proc. R. Soc. Lond. A* 340, 471–493.
- Løvholt, F., Glimsdal, S., Lynett, P., Pedersen, G., 2015. Simulating tsunami propagation in fjords with long-wave models. *Nat. Hazards Earth Syst. Sci.* 15, 657–669.
- Miles, J.W., 1977a. Obliquely interacting solitary waves. *J. Fluid Mech.* 79, 157–169.
- Miles, J.W., 1977b. Resonantly interacting solitary waves. *J. Fluid Mech.* 79, 171–179.
- Mori, N., Takahashi, T., Yasuda, T., Yanagisawa, H., 2011. Survey of 2011 Tohoku earthquake tsunami inundation and run-up. *Geophys. Res. Lett.* 38, L00G14.
- Pakoksung, K., Suppasri, A., Imamura, F., Athanasius, C., Omang, A., Muhari, A., 2019. Simulation of the submarine landslide tsunamis on 28 September 2018 in Palu Bay, Sulawesi island, Indonesia, using a two-layer model. *Pure Appl. Geophys.* 176, 3323–3350.
- Perroud, P., 1957. The solitary wave reflection along a straight vertical wall at oblique incidence. *IER Rep.* 99, 93.
- Pudjaprasetya, S., Adytia, D., Subasita, N., 2021. Analysis of bay bathymetry elements on wave amplification: A case study of the tsunami in Palu Bay. *Coast. Eng. J.* 63, 433–445.
- Romano, A., Bellotti, G., Di Risio, M., 2013. Wavenumber–frequency analysis of the landslide-generated tsunamis at a conical island. *Coast. Eng.* 81, 32–43.
- Romano, A., Lara, J.L., Barajas, G., Losada, I.J., 2023. Numerical modeling of tsunamis generated by granular landslides in OpenFOAM®: A Coulomb viscoplastic rheology. *Coast. Eng.* 186, 104391.
- Ruffini, G., Heller, V., Briganti, R., 2019. Numerical modelling of landslide-tsunami propagation in a wide range of idealised water body geometries. *Coast. Eng.* 153, 103518.
- Ruffini, G., Heller, V., Briganti, R., 2021. Numerical characterisation and efficient prediction of landslide-tsunami propagation over a wide range of idealised bathymetries. *Coast. Eng.* 167, 103854.
- Stelling, G.S., Duijnmeijer, S.A., 2003. A staggered conservative scheme for every Froude number in rapidly varied shallow water flows. *Internat. J. Numer. Methods Fluids* 43, 1329–1354.
- Stelling, G., Zijlema, M., 2003. An accurate and efficient finite-difference algorithm for non-hydrostatic free-surface flow with application to wave propagation. *Internat. J. Numer. Methods Fluids* 43, 1–23.
- SWASH, T., 2020. SWASH user manual version 7.01. Delft University of Technology. Environ. Fluid Mech. Sect.
- Tanaka, M., 1993. Mach reflection of a large-amplitude solitary wave. *J. Fluid Mech.* 248, 637–661.
- Teng, M.H., 1997. Solitary wave solution to Boussinesq equations. *J. Waterw. Port Coast. Ocean Eng.* 123, 138–141.
- Teng, M.H., Wu, T.Y., 1992. Nonlinear water waves in channels of arbitrary shape. *J. Fluid Mech.* 242, 211–233.
- Wuppukondur, A., Baldock, T., 2022. Physical and numerical modelling of representative tsunami waves propagating and overtopping in converging channels. *Coast. Eng.* 174, 104120.
- Xian-chu, C., 1981. The solitary waves in a gradually varying channel of arbitrary cross-section. *Appl. Math. Mech.* 2, 429–440.
- Xue, H., Ma, Q., Diao, M., Jiang, L., 2019. Propagation characteristics of subaerial landslide-generated impulse waves. *Environ. Fluid Mech.* 19, 203–230.
- Zhang, Y., Li, D., Chen, L., Yin, K., Xiao, L., Fu, X., Glade, T., Leo, C., 2020. Numerical analysis of landslide-generated impulse waves affected by the reservoir geometry. *Eng. Geol.* 266, 105390.
- Zijlema, M., 2020. Computation of free surface waves in coastal waters with SWASH on unstructured grids. *Comput. & Fluids* 213, 104751.
- Zijlema, M., Stelling, G.S., 2005. Further experiences with computing non-hydrostatic free-surface flows involving water waves. *Internat. J. Numer. Methods Fluids* 48, 169–197.
- Zijlema, M., Stelling, G., Smit, P., 2011. SWASH: An operational public domain code for simulating wave fields and rapidly varied flows in coastal waters. *Coast. Eng.* 58, 992–1012.
- Zitti, G., Ancey, C., Postacchini, M., Brocchini, M., 2016. Impulse waves generated by snow avalanches: Momentum and energy transfer to a water body. *J. Geophys. Res.: Earth Surf.* 121, 2399–2423.